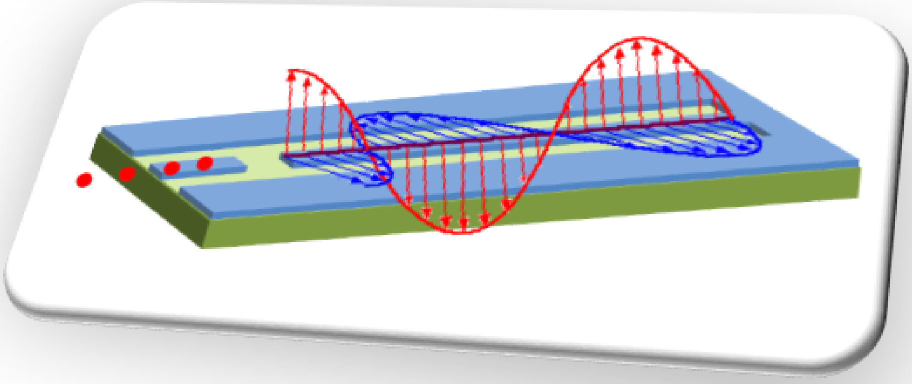

Single Photon Characterization of (103)-oriented $YBa_2Cu_3O_{7-x}$ Coplanar Waveguide Resonator

Thesis for the Degree of Erasmus Mundus Master of Nanoscience and Nanotechnology

CHIRAG MURENDRANATH PATIL

Examiner: Prof. Samuel Lara Avila
Supervisor: Prof. Thilo Bauch & Prof. Floriana Lombardi
KU Leuven Co-promotor: Prof. Victor Moshchalkov

Department of Microtechnology and Nanoscience
CHALMERS UNIVERSITY OF TECHNOLOGY
Gothenburg, Sweden 2015

Master's thesis 2015

This thesis was conducted under the program
Erasmus Mundus Master of Nanoscience and Nanotechnology
with Nanoelectronics trajectory
Katholieke Universiteit Leuven (Belgium)
Chalmers tekniska högskola (Sweden)

Single Photon Characterization of (103)-oriented $YBa_2Cu_3O_{7-x}$ Coplanar Waveguide Resonator

Chirag Murendranath Patil

Supervisors :
Floriana Lombardi & Thilo Bauch
September 2015

Quantum Device Physics Laboratory
Department of Microtechnology and Nanoscience
Chalmers University of Technology
Gothenburg, Sweden 2015

Single Photon Characterization of (103)-oriented $YBa_2Cu_3O_{7-x}$ Coplanar Waveguide Resonator
CHIRAG MURENDRANATH PATIL

Supervisor: Prof. Thilo Bauch & Prof. Floriana Lombardi
Examiner: Prof. Samuel Lara Avila
KU Leuven Co-promotor: Prof. Victor Moshchalkov

Master's Thesis 2015
Quantum Device Physics Laboratory
Department of Microtechnology and Nanoscience
Chalmers University of Technology
SE-412 96 Gothenburg
Telephone +46 31 772 1000

Cover: Photons entering into a quarter wavelength coplanar waveguide resonator.

Typeset in $\LaTeX$
Printed by [Chalmers Reproservice]
Gothenburg, Sweden 2015

Abstract

The strong electron-electron correlation makes the cuprate high critical-temperature superconductors (HTS) to behave as unconventional metals, where conventional electron band theory fails to describe the various electronic and magnetic properties of these materials. The most prominent property of HTSs is the superconducting state, whose order parameter symmetry is known to be dominated by a d-wave [1]. Up to date no microscopic theory exists, which could explain the occurrence of superconductivity in these materials. However, the low energy quasiparticle excitation spectrum in these materials is believed to hold key information about the microscopic mechanism leading to the phenomenon of superconductivity in HTS [2].

Superconducting quantum devices are powerful tools to study the quasiparticle excitation spectrum. In fact, a tiny fully developed superconducting gap ($20\mu eV$) has been observed by studying the electronic transport in an all-HTS single electron transistor [2]. This experiment unveiled a subdominant complex (s-wave) part in the order parameter besides the d-wave component. A complementary experiment thereof would be the study of relaxation times in a HTS transmon qubit, which should scale with the quasiparticle density of states in the HTS material.

The transmon is a type of artificial two-level system (TLS), realized by a capacitively shunted Josephson junction, which is embedded in a superconducting resonator. By probing the microwave spectrum of this two-level system using single photons inside the resonator one can obtain information about quasiparticle induced relaxation processes in the TLS at the qubit transition frequency. Here the resonator acts like a filter towards the environment protecting the transmon from any noise source outside the resonator. Since this device is operated at higher frequencies (around 5 Ghz, which corresponds to an energy of $20\mu eV$), it is characterized at corresponding low temperatures ($T \approx 120mK$). The key ingredient of the HTS transmon is the Josephson junction. High quality junctions using HTS can be realized using the bi-epitaxial grain boundary junction. Here, the junction is localized at the interface of (001) oriented YBCO and a (103) oriented YBCO electrode.

In order to study quasiparticle induced relaxation processes in a YBCO transmon, all other loss mechanisms such as dielectric losses of the substrate and conductor losses of the YBCO need to be known and characterized in advance. The microwave properties of (001) YBCO films are studied and fairly well understood [3], whereas the microwave properties of (103) YBCO films are yet to be revealed; especially in the low temperature and low power limit (single microwave photon limit). So it is appropriate to study the high frequency dissipation properties of YBCO in the framework of the transmon.

By patterning a resonator device using (103) YBCO, its microwave dissipation properties can be investigated within the scope of the transmon design i.e, measuring in the millikelvin temperature and probing in the single photon limit. In this thesis, the resonator is implemented adopting a *Coplanar waveguide* (CPW) design to understand the different loss mechanisms in the preceding context. The temperature dependence of the resonance frequency and the quality factor (of CPW) is then related to the available models describing various dissipation mechanisms.

This work is further directed towards exploring the possibilities of using this CPW resonator as a sensitive magnetic field sensor. This is achieved by studying the variation of the (kinetic) inductance of the superconductor by applying an external magnetic field and also performing some noise measurements to determine its sensitivity. These tasks are the main focus of this thesis work. The first chapter gives a brief introduction to the phenomenological aspects of superconductivity, modeling and design of the coplanar waveguide resonator and properties of a superconducting microwave resonator. Chapter 2 gives a catalogue of the various clean room process steps involved in the fabrication of the resonator followed by the high frequency measurement setup to probe the resonator device. The measured results are analyzed and discussed with conclusion in the final chapters.

Keywords: Transmon, YBCO, High Tc superconductors, d-wave, quasiparticle spectrum analysis, kinetic inductance, london penetration depth, quality factor, coplanar waveguide resonator.

Acknowledgements

This thesis was carried out under the programme, Erasmus Mundus Master in Nanoscience and Nanotechnology (EMM NANO) jointly organised by a consortium of four universities. My first year was at KU Leuven, BELGIUM and second year at Chalmers University, SWEDEN. This thesis would not have been possible without the guidance of many people. First, I would like to thank my supervisors, Prof. Thilo Bauch and Prof. Floriana Lombardi for giving me an opportunity to learn and work on this literally COOL Master thesis research project. Being an exchange student, finding a thesis topic in a field of my interest was a daunting task. But after attending few lectures of Thilo on Quantum Informatics, the concept of superconducting qubits captivated my interest.

I would like to thank Marco, who was my mentor, friend and partner in making our hands dirty in the clean room. Thanks to Riccardo for his help with the XRD measurements and ever green quick witticism, Reza who helped with Titanium deposition and thoughtful insights and to Luca who patiently waited till we were done with our measurements. I would like to thank the cleanroom faculty at MC2 who have been imparting their secrets on various tools and equipments. Thanks to QDP for the very many fika and the pep talks. I'm grateful for the support from all my family and friends who have always encouraged me and believed in my abilities.

Chirag M Patil, Gothenburg, September 2015

Contents

List of Figures

1

Literature review

Superconductivity is a macroscopic quantum phenomenon which was discovered on April 8, 1911 by Dutch physicist Heike Kamerlingh Onnes in Leiden when he noticed that the resistance of mercury abruptly reduced to zero at about 4K [4]. The materials which exhibited superconductivity showed exactly zero electrical resistance and expulsion of magnetic fields (*Meißner-Ochsenfeld effect*) when cooled below a transition temperature. This temperature is a characteristic property of the material and for many years since its discovery, had remained close to a few degree Kelvin. However, owing to their fascinating properties, superconductors could have a strong impact on several applications. For instance, they could be employed to transmit electric energy over long distances without any power loss and further even levitating trains. Indeed, scientists were further motivated to find new materials which turned superconducting at higher critical temperature or even close to room temperature. Recently, a giant leap for the research community was made when superconductivity was observed at a record high temperature of $203K$ in samples of hydrogen sulfide subjected to extremely high pressure [5].

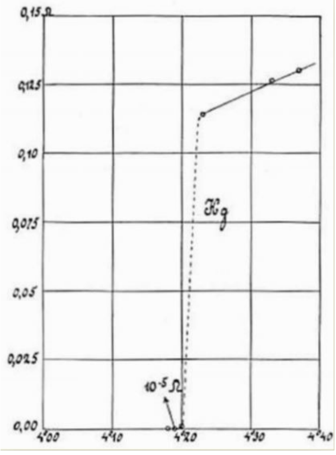

Figure 1.1: Historical plot of resistance(ohm) vs. temperature(Kelvin) showing the transition temperature of 4.2K for Mercury [4].

It wasn't until 1986, that researchers Bednorz and Müller discovered that certain Ba-doped ceramic cuprates became superconducting at relatively high temperatures [6]. Soon $YBa_2Cu_3O_{7-x}$, the first superconductor with a transition temperature ($Tc \sim 90K$) above boiling point of liquid nitrogen, was discovered by P. Chu and others [7]. Such high transition temperatures could not be correlated to the theory of conventional superconductors and hence they came to be known as *high* *critical temperature superconductors* (HTS). Over the course of time, tremendous advancements were made in this field and new materials with much higher critical temperatures are found. These compounds were investigated extensively and interesting properties were scrutinized, but a microscopic theory describing these unusual properties has not yet been fully developed.

1.1 Macroscopic theory of superconductivity

Little was known about the mechanisms behind superconductivity for almost half a century since its discovery, before anyone came up with a microscopic theory. Prior to the microscopic theory, two successful phenomenological theories were formulated. Fritz and Heinz London first explained the superconducting phenomena by applying Maxwell's equations to dissipation-less charge carriers in and around a superconductor [8]. The Ginzburg-Landau (GL) theory is another phenomenological model which describes the macroscopic behaviour of superconductors and provides a framework to understand this phenomenon [9]. This theory is of great importance from the thermodynamics aspect of superconducting phase transition. Ginzburg and Landau asserted that the transition to the superconducting state is a second order phase transition and the free energy F_s of the superconductor near the phase transition can be expressed in terms of a complex order parameter Ψ. This order parameter can be defined as below.

$$\Psi = \begin{cases} = 0, & \text{for } T > T_c \\ \neq 0, & \text{for } T < T_c \end{cases} \tag{1.1}$$

In the superconducting state, the concentration of superconducting charge carriers (superfluid) can serve as the order parameter. Thus, the modulus of the order parameter depends on temperature and describes the density of superconducting electrons i.e, $|\Psi|^2 = \Psi\Psi^* = n_s(r)$. In the vicinity of temperature below T_c, the total free energy describing the second order phase transition can be expanded in terms of order parameter[1] as:

$$F_s = F_n + \alpha(\Psi)^2 + \frac{\beta}{2}(\Psi)^4 + \frac{1}{2m^*}|(-i\hbar\nabla - 2e\mathbf{A})\Psi|^2 + \frac{|\mathbf{B}|}{2\mu_0} \tag{1.2}$$

where, F_n is the free energy in the normal state, α and β are the phenomenological parameters, m^* is the effective mass, e is the charge of an electron, $\mathbf{A}$ is the vector potential and $\mathbf{B} = \nabla \times \mathbf{A}$ is the applied magnetic field. If one considers the situation in presence of magnetic field and minimize the free energy with respect to spacial variation of order parameter Ψ and the vector potential $\mathbf{A}$, one can arrive at the GL equations as

$$\begin{aligned} \alpha\Psi + \beta|\Psi|^2\Psi + \frac{1}{2m^*}(-i\hbar\nabla - 2e\mathbf{A})^2\Psi = 0 \\ j_s = \frac{ie\hbar}{2m}\left(\Psi^*\frac{\partial}{\partial r}\Psi - \Psi\frac{\partial}{\partial r}\Psi^*\right) - \frac{2e^2}{m}\Psi^*\mathbf{A}\Psi \end{aligned} \tag{1.3}$$

---

[1] This is valid only if Ψ is small and has small spatial variations.

The first equation with its nonlinear term determines the order parameter Ψ. Ψ and $\mathbf{B}$ are related by Ampere's law: $(\partial/\partial r) \times \mathbf{B} = \mu_0 j_s$, where j_s denotes the supercurrent density. The second GL equation can take into account the supercurrents for a spatially varying wave function. These GL equations also predicted two new characteristic lengths at the vicinity of a superconducting surface. The *London penetration depth*, λ is a length scale characterizing how the magnetic field penetrates into the superconducting region. The magnetic field decays, within a distance λ inside the bulk, to a value of $\frac{1}{e}$ times its value at the surface. Using the parametric terms of GL model, it can be derived as

$$\lambda_{GL}(T) = \sqrt{\frac{m\beta}{\mu_0 e^2 \alpha(T)}} \tag{1.4}$$

Another length scale, the *Coherence length*, ξ can also be evaluated from this model. It reveals how the order parameter at the normal-superconductor interface develops from zero and reaches its full value deep within the superconducting bulk. This natural length scale for spatial variation of the order parameter can be derived as

$$\frac{1}{\xi_{GL}^2(T)} = \frac{2m|\alpha(T)|}{\hbar^2} \tag{1.5}$$

The GL equation shows that when a magnetic field penetrates the superconducting region, it increases the free energy of the system, where as the order parameter developed over coherence length causes the free energy to decrease because of evolution of order. These two are competitive factors and the sum of these two contributions decides the relative balance of the normal and superconducting free energy densities. This gives rise to two different possibilities.

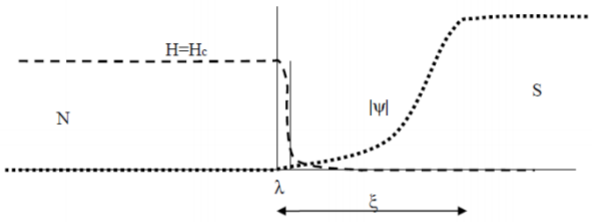

Type I superconductor

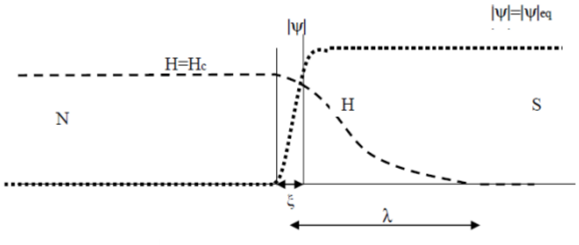

Type II superconductor

Figure 1.2: Relationship between the London penetration depth and Coherence length for Type I and Type II superconductors [10]

If the London penetration depth is longer than the coherence length, the spatial variation of the order parameter can be ignored and as a result the total free energy is positive. On the other hand, if london penetration is smaller than the coherence lenghts, one can neglect the increase of free energy due to magnetic field and conclude that the total energy of the system is negative. Accordingly, this temperature independent ratio[2] can be defined as

$$\kappa = \frac{\lambda(T)}{\xi(T)} \tag{1.6}$$

where κ is the *Ginzburg Landau parameter*. There can be two type of superconducting materials with positive and negative energies. A superconductor is called *Type I* if $\kappa < \frac{1}{\sqrt{2}}$ and *Type II* if $\kappa > \frac{1}{\sqrt{2}}$.

In Type I material, the magnetic flux is excluded with negative magnetisation in the superconducting state region, and at the thermodynamic critical field, the flux penetrates completely and material behaves normal.

In type II material, there is partial penetration of magnetic flux in the field region between lower and upper critical fields (mixed state). Here, GL theory tries to explain how normal and superconducting states can coexist in mixed state. A mixed state can exist if it is energetically favorable to produce an interface where normal and superconducting regions are separated by a surface. This is only possible if free energy of the system is lowered by the creation of such an interface. Essentially the free energy balance is determined by the two characteristic length scales, london penetration and coherence lengths.

Both these characteristic lengths can be determined experimentally, hence κ can be calculated to verify Type I and Type II superconducting materials. The GL theory provides a guideline for describing practical Type II superconductors which has its real interest in technical applications, however provide no information on what happens at the microscopic scale. A microscopic theory was further developed in 1957 which described the microscopic pairing interaction illustrating the mechanism of superconductivity.

1.2 Pair condensate and BCS microscopic theory

BCS theory is the first theory of superconductivity which employed a quantum mechanical approach to describe this phenomenon at a microscopic scale [11]. The authors John Bardeen, Leon Cooper, and John Robert Schrieffer together received the Nobel Prize in Physics for this theory in 1972. A key concept in this theory is the pairing of two electrons which are bound together below a certain critical temperature to form a coherent state called *Cooper pair*. The superconducting electrons collectively occupy the lower energy ground state compared to that in the normal state. Since it is a macroscopic phenomena, all the Cooper pairs can be characterized by a single position dependent complex order parameter Ψ which is given by:

---

[2] Calculations from the microscopic theory gives a weak temperature dependence for κ.

$$\Psi(\hat{r}) = \sqrt{n_s}e^{i\theta.} \tag{1.7}$$

In this expression, n_s is the average density of paired electron condensate, and θ is the quantum mechanical phase. There are no allowed energy states in the energy spectrum for the Cooper pair to scatter. Thus Cooper pair reflects the dynamics of a dissipationless scattering.

For superconductivity, the atomic arrangement influences more than the atomic behaviour in the lattice[3]. It follows that electrons interact with the crystal lattice and condense into the ground state forming the Cooper pair. The nature of interaction which causes the electrons to pair up is attractive and is mediated by dynamic phonon distortion. However, the net attractive potential energy should be greater than the repulsive coulombic energy between the electrons. As a result, the electrons condense into an ordered state and usually this coherence extends over distances greater than the atomic separation.

The pair formation is the essence of BCS theory. The effective net attraction between the electrons produces a superconducting gap Δ (meV) in the electronic band structure, which keeps them paired. These pairs do not undergo scattering as long as the thermal energy of the system is less that this *binding energy*. Ergo, current flows without any resistance i.e, superconductors have zero DC resistance. Superconductivity occurs only below a critical temperature, which is related to the energy gap size.

$$2\Delta \approx 3.5k_BT_c \tag{1.8}$$

Above the critical temperature, pairing cannot occur and resistance can be observed. For low critical temperature superconductors, this superconducting gap can be expressed by Equation 1.8 and near the critical temperature as:

$$\frac{\Delta(T)}{\Delta(0)} = 1.74\left(1 - \frac{T}{T_c}\right)^{0.5} \tag{1.9}$$

As one approaches the critical temperature, this binding energy weakens and becomes zero. At finite temperatures, the condensate is broken down by the thermal phonons forming elementary excitations called *Bogoliubov quasiparticles*. These are different from conventional quasiparticles found in metals, since they have combined features of both electron and hole excitations. The energy required to break one Cooper pair is 2Δ. Now the superconducting bulk consists of both quasiparticles and Cooper pairs and the dynamics of the charge carriers is no more dissipationless. The existence of quasiparticles in superconductors results in dissipation under the influence of high frequency electro-magnetic fields. An important validation of the BCS theory was to experimentally measure this gap and compare the value obtained with that predicted.

---

[3] White, metallic tin is a superconductor whereas grey, semiconducting tin is not.

1.3 Conventional vs. Unconventional Superconductivity

The superconducting gap can be determined experimentally using different techniques such as tunneling effect and specific heat measurements [12]. The higher the critical temperature, the larger is the value of this gap. The BCS also shows that this gap increases with the interaction energy strength between electrons in Cooper pair. Weakly-coupled electrons in low-temperature superconductors usually follow Equation 1.8. In strongly correlated systems, electrons are closely associated with atomic orbitals and retain their localized nature. The wave function of a two identical fermions pair is *antisymmetric* with respect to the exchange of the two electrons involved[4]. There can be two possibilities arising from this. i) Orbital component of wave function is symmetric (orbital angular momentum L=0,2,... which corresponds to s-wave, d-wave,...) and spin component is antisymmetric (spin singlet). ii) Orbital component of wave function is antisymmetric (orbital angular momentum L=1,3,... which corresponds to p-wave, f-wave,...) and spin component is symmetric (spin triplet). BCS considers spin singlet coupling, and hence the allowed orbital wave functions for a BCS superconductor would be s-wave, d-wave and so on. One can now define a conventional superconductor as a condensate of L=0 Cooper pairs, i.e. the most symmetric pairing state. For s-wave conventional superconductors, S=0 and L=0. So in order to produce excitations across the gap, the same energy 2Δ is required in all k-space direction, i.e, there are no nodes and the gap is found to be symmetric about the fermi level in all momentum space directions (isotropic).

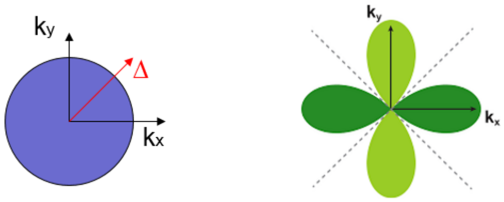

s-wave d-wave

Figure 1.3: Variation of the energy gap function corresponding to isotropic s and $d_{x^2-y^2}$ symmetry of the order parameter in the momentum space.

Unconventional superconductors are all other states with orbital angular momentum L>1. The order parameter symmetry is not s-wave. In High critical temperature superconductors (HTS) such as cuprates, the gap is found to be anisotropic and exhibits symmetries with different shapes. Knowledge about the underlying symmetry is important to unravel the origins of the pairing mechanism in these materials. Direct evidences pointing at the d-wave order parameter in cuprates can be found in Josephson junction dynamics measurements and magnetic field dependence of London penetration depth measurements [13][14]. It was also suspected that low energy quasi particles along the nodes in $d_{x^2-y^2}$ make it impossible for

---

[4] in accordance with Pauli exclusion principle

observing macroscopic quantum behaviour. However, recent experiments demonstrated macroscopic quantum effects in HTS junctions [15]. This opened up new research exploring the possibility of an admixture of pure d-wave wavefunction with additional imaginary components of s-wave in the order parameter of HTS [16]. The behaviour of low energy quasi-particle excitations can throw light on the phase transitions and superconducting mechanism of high temperature superconductors.

1.3.1 High critical temperature superconductor-cuprates

The discovery of superconductivity in certain pervoskite-type layered cuprates by Bednorz and Muller [17] has been the subject of research since decades, while researchers are still trying to figure out the microscopic theory explaining superconductivity at high temperatures. The common HTS are compounds of copper and oxygen, so called cuprates, which encompass almost thirty distinct crystalline structures and contain more than three different elements. One of the common features in their structures is the layer structure of copper oxide planes which holds the key for mobile charge carriers in HTS. Without any oxygen doping, these compounds are typically insulators with antiferromagnetic order and are not metals. The magnetic moment on the copper site alternates as one moves from one site to the next. In order to make the compound metallic and subsequently superconducting, oxygen is usually doped between the copper oxide planes. By adding oxygen to the copper chains, some free carriers are released which can contribute towards charge transport. The antiferromagnetism then disappears and the material becomes a metallic superconductor. There have been certain theories trying to explain HTS such as antiferromagnetic spin fluctuation mechanism which is still under active development [18].

The metallic behaviour that arises is characterised by significant anisotropy. The anisotropic structure of these compounds is reflected in the anisotropy of the relevant intrinsic electronic properties of these materials such as london penetration depth and coherence lengths [19]. Also, the electrical resistance along c-axis could be thousand times higher than the resistance for currents carried in ab-plane. The observation of strong anisotropy in these physical properties does not substantiate the claim whether the HTS are two-dimensional like metals or a form of anisotropic three-dimensional crystal structures. However, there are strong evidence to prove the confinement of mobile charge carriers in the copper oxide planes [19] which contribute towards electron transport. This has very huge implications on the origins of superconductivity in HTS materials.

The CuO_2 layers in cuprates can be considered as the source of superconductivity in HTS materials. Consequently, the pairing symmetry also reflects the symmetry of the CuO_2 planes. Further, the $d_{x^2-y^2}$ orbital state of the Cu^{2+} ions, suggest that electron-electron interactions are more significant than electron-phonon interactions in cuprates, making this kind of superconductivity unconventional.

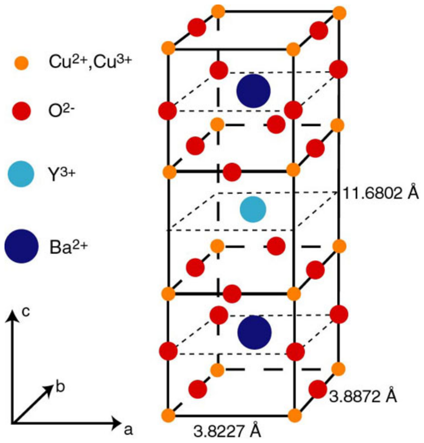

Figure 1.4: Structure of $YBa_2Cu_3O_{7-x}$ unit cell [20]

1.3.2 Crystal structure of YBCO

The complex, multi-layered crystalline structure of YBCO makes it difficult to arrive at a theory explaining the mechanism of superconductivity in these materials. The YBCO falls into the crystallographic family called perovskites with its pseudocubic elementary perovskite unit cells as shown in Figure 1.4.

The compound $YBa_2Cu_3O_{7-x}$ has orthorhombic symmetry (for x=0) and the structure has two Cu-O sheets in ab plane and Cu-O chains along the b-axis. A unit cell contains a layer of Cu-O with four oxygen ions surrounding a Cu(I) atom, then a layer of BaO, a layer of Cu-O with five oxygen ions surrounding Cu(II) atom forming a polyhedron and lastly a layer of yttrium short of four oxygen. The stacking sequence of the ab planes is CuO–BaO-CuO_2–Y–CuO_2–BaO–CuO with Cu-O chains along the b-axis.

One of the key features is the presence of two CuO_2 layers which are responsible for the transport of mobile charge carriers. The Yttrium atom acts as a spacer between these two layers, and also serves as a charge reservoir. The presence of oxygen atoms in these chains is essential for superconductivity and the lattice parameter varies with oxygen content. However, there are a number of oxygen vacancies in the lattice and hence is referred to as an oxygen deficient perovskite structure.

As can be seen from the phase diagram, there are different phases and magnetic order which can be tuned by doping. The phase diagram in Figure 1.5 shows that YBCO is in the antiferromagnetic phase when the doping is close to zero. As the oxygen content is increased to the ideal doping value, it changes to superconducting phase. The psuedogap temperature T^* is another prominent feature of YBCO. It is usually observed in the underdoped regime (lower carrier concentration) for p-doped YBCO. This temperature is more of a crossover than a phase transition, where specific features in the electrical, magnetic, and optical properties are observed. It is still unclear if this pseudogap is due to the fluctuations in the dielectric or the superconducting nature [4]. The value of x in a particular sample depends on the processing conditions, especially temperature and oxygen partial pressure. For $x \geq 0.6$ the structure becomes tetragonal and thus for x=1, $YBa_2Cu_3O_6$ has no oxygen in the chain and Cu in b-axis now is in the +1 state and is non-superconducting.

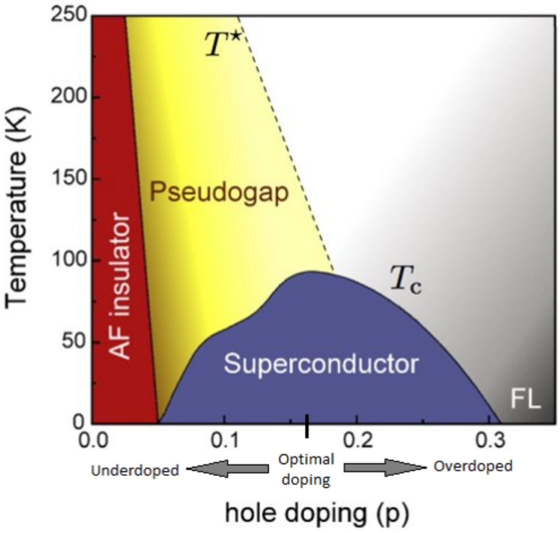

Figure 1.5: The YBCO Phase diagram showing various transitions. [21]

The critical temperature Tc of $YBa_2Cu_3O_{7-x}$ also varies with x-value. Structural studies have revealed that oxygen vacancies may be ordered when x = 0.5 and 0.75 [1].

1.4 Description of a CPW resonator

In this section, the modelling and designing of a resonator in the GHz-regime is illustrated employing the coplanar waveguide (CPW) technology. For this thesis, the CPW design was chosen over other transmission lines because of its simplicity and minimum fabrication steps involved. Since a superconducting CPW is at stake, additional process steps might damage the thin film changing the quantities which determine microwave losses, namely its surface resistance and penetration depth. Also fabricating a CPW device with superconducting materials, high current densities can be achieved with negligible attenuation and high quality factor values.

1.4.1 Coplanar transmission waveguide

Coplanar waveguide is a type of electrical transmission line which can be fabricated using circuit board technology as well as microfabrication processing technology. It is used to propagate microwave frequency signals and also study the properties of the material and devices. This technique was first demonstrated by C. P. Wen, who successfully fabricated a CPW on a dielectric substrate [22]. A CPW consists of a semi-infinite central conductor separated by microscopic gaps from the ground plane on either sides.

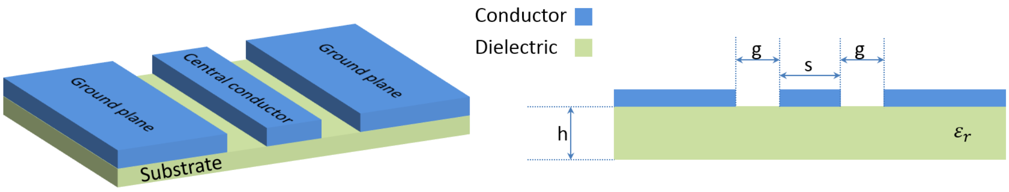

a. CPW top view

b. CPW cross section view

Figure 1.6: Coplanar waveguide structure.

However, the electric and the magnetic fields propagating in the central line should satisfy a set of restricting conditions. For deriving analytical approximations of the CPW resonator with some reasonable accuracy, conformal mapping technique is used as in reference [23]. A capacitor in the form of interdigitized fingers is used to achieve a good coupling from the input port to the main CPW structure. Microwave photons are injected into the CPW through this finger capacitance. The value of this coupling capacitance are calculated by performing conformal mapping techniques on its length features.

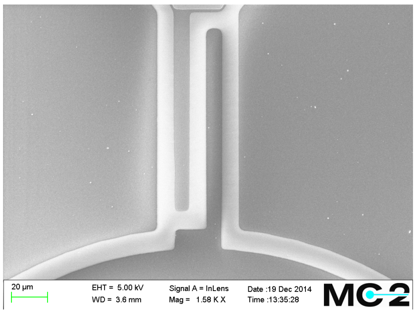

Figure 1.7: SEM image of the finger capacitor used to probe the CPW resonator.

Each of the finger capacitor has a width of $s_f = 8\mu m$ and is spaced at $g_f = 10\mu m$. By changing the finger lengths, different orders of coupling can be achieved which allows to have control over the external losses. The total coupling capacitance can be evaluated from the formula

$$C_f = 2l_f\epsilon_0\epsilon_{eff}\left(\frac{K_{01}}{K_0}\right) \tag{1.10}$$

where l_f is the finger length, ϵ_0 is the dielectric constant of air, ϵ_{eff} is the effective dielectric constant and K_{01}, K_0 are the elliptic integrals of the first kind with their modules k_{01}, k_0 determined from finger's geometry. The total capacitance of the CPW is nothing but the sum of partial capacitance of the finger structure and that of the CPW design.

Similarly, the characteristic parameters of the resonator design are derived analytically from conformal mapping method [23]. The cross section view of a CPW structure on a single dielectric substrate is as shown in figure 1.6.

The center strip conductor has a width $s = 20\mu m$ separated from the ground plane at a gap distance of $g = 24\mu m$. The height of the dielectric substrate is

$h = 0.5mm$ with the corresponding dielectric constant $\epsilon_r = 23$. From this geometry, the total inductance per unit length L_{tot} has to be calculated and is given by $\phi^{‘}/I$ where $\phi^{‘}$ is the magnetic flux per unit length and I is the current through the CPW line. Here, $\phi^{‘}$ is a combination of flux thought the CPW line and flux between the gap. Hence, the total inductance incorporates both external inductance L_{ex} and kinetic inductance L_{kin}, which is by virtue of inertia of superconducting electrons. By using conformal mapping techniques similar to the ones proposed before, the external inductance per unit length is calculated as

$$L_{ex} = \frac{\mu_0}{4}\left(\frac{K_{01}}{K_0}\right) \tag{1.11}$$

where K_{01} and K_0 are the complete elleptic integrals with their modules calculated from the CPW geometry. Similarly, the kinetic inductance [5] per unit length has also been evaluated analytically by comparing the partial wave analysis results [24].

$$L^{'}_{kin} = \mu_0\lambda_L \frac{C}{4ADK_0}\left(\frac{1.7}{\sinh\left[t/2\lambda_L\right]} + \frac{0.4}{\sqrt{[(B/A)^2-1][1-(B/D)^2]}}\right) \tag{1.12}$$

where $A, B, CandD$ are different dimension dependent parameters which can be referred to in the source [24]. λ_l is the london penetration depth of the superconducting material. With this approximation, the total inductance per unit length of the CPW can be calculated as $L_{tot} = L_{ex} + L_{kin}$. The total capacitance can be mapped as a parallel configuration of partial capacitances at various interfaces. Further, the total capacitance per unit length can be deduced as:

$$C_{tot} = 4\epsilon_0\epsilon_{eff}\frac{K_0}{K_{01}} \tag{1.13}$$

By adjusting the gap and conductor dimensions, the characteristic impedance Z_0 of the CPW can be customized to be around 50Ω which is the standard value for the coaxial cables used in the measurement setup. For small losses, applying the values of total capacitance and inductance per unit lengths evaluated earlier; the characteristic impedance of the superconducting transmission line can be calculated as

$$Z_0 = \sqrt{\frac{L_{tot}}{C_{tot}}} \tag{1.14}$$

---

[5] Kinetic inductance is the manifestation of the inertial mass of Cooper pairs in superconductors, similar to series inductance in normal conductors.

1.5 Microwave resonator

A resonator is a useful microwave device which offers a high impedance to the source at a specific operating frequency. This frequency is called as its *resonant frequency* and defines the rate at which resonator transforms the stored energy from kinetic to potential energy and vice-versa. Such resonators can be built either using distributed or lumped elements. In lumped element resonators, the capacitor stores electrical energy (kinetic energy) and inductors stores the magnetic energy (potential energy). Any dissipation losses can be represented by a resistor.

In case of distributed resonance circuits, resonance occurs in the form of standing waves due to the superposition of forward moving and reverse travelling wave. Any form of transmission lines with suitable lengths can be used a resonator with appropriate boundary conditions. Here, a transmission line in the form of a coplanar waveguide is used, hence *CPW resonator*.

Researchers have been exploiting the unique properties of high T_c superconductors for implementing high frequency circuits such as feed lines, resonators and radar systems. For this, thin films patterened on microwave substrates have to be evaluated to determine their quality factor, london penetration, surface resistance and other loss mechanisms prior to developing microwave circuits. Here, the physical properties of a co-planar waveguide resonator and its relation to the material properties of the superconductor is discussed.

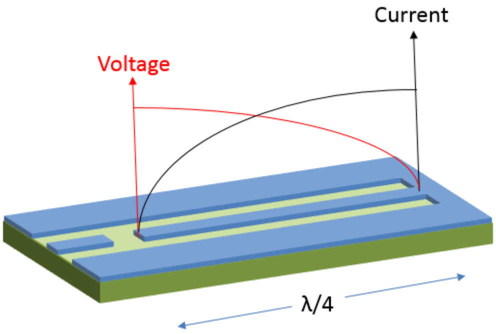

Figure 1.8: Illustration of a quarter wavelength coplanar waveguide resonator

A basic representation of coplanar waveguide structure is as shown in Figure 1.8 which consists of a center strip conductor with semi infinite ground planes on either sides. Depending on the boundary conditions, a λ, $\lambda/2$ or a $\lambda/4$ resonator can be designed. Here, a $\lambda/4$ or a quarter wave resonator is designed by shorting one end of the center line to the ground plane and keeping the other end open. For a $\lambda/4$ resonator, the only allowed electromagnetic modes will have a wavelength $\lambda = 4l/(2m+1)$, where l is the length of resonator and m is an integer.

The interesting feature of fabricating CPW with superconducting materials is that high current densities can be achieved with negligible attenuation which allows for high quality factor values compared to normal conductor resonators. This allows to fabricating sensitive resonators with high accuracy of designed resonance frequency values. Epitaxially grown (103)-YBCO $\lambda/2$ resonator is patterned using techniques which are described in the subsequent chapter.

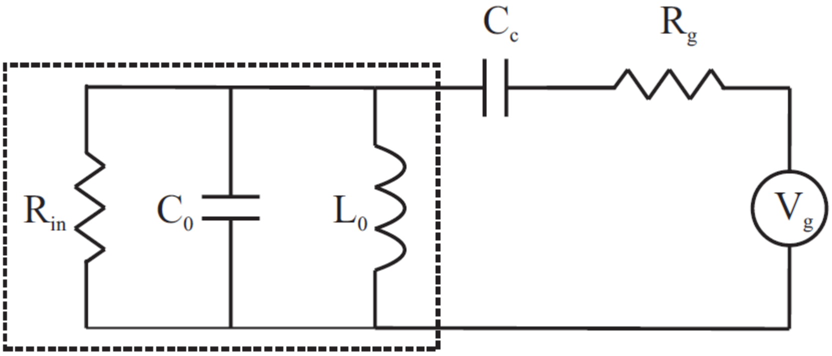

Figure 1.9: Lumped element circuit diagram of a resonator.

The equivalent circuit of a quarter wavelength CPW resonator can be considered as a shunt of lumped elements, inductor and capacitor as seen in Figure 1.9. It is an energy storing element where energy oscillates between the capacitance and the inductance segment with a resonant frequency, f_0 [Hz], given by:

$$f_0 = \frac{1}{2\pi\sqrt{L_0 C_0}} \tag{1.15}$$

where L_0 is the lumped element inductance (H) and C_0 is the shunt capacitance (F). These lumped element parameters can be calculated from the transmission line parameters C' and L'.

$$\begin{aligned} C_0 &= \frac{C'l}{2} \\ L_0 &= \frac{8L'l}{\pi^2} \\ R_0 &= \frac{Z_0}{\alpha l} \end{aligned} \tag{1.16}$$

Here, Z_0 is the characteristic impedance of the CPW. Another feature of the CPW resonator is its quality factor, which is an indicator of the energy losses in the resonator, and can be defined as:

$$Q = \frac{\text{Energy stored}}{\text{Energy dissipated per cycle}} \tag{1.17}$$

The resonator circuit is driven by an external RF signal. When this frequency is close to the resonance frequency of the resonator f_0, the energy of the probing signal is absorbed. The resonance curve is obtained by measuring the reflection coefficient at different frequencies. The reflection coefficient is a parameter which compares the incoming and the outgoing signals in a resonator. It is typically represented by Γ and is expressed as:

$$\Gamma = \frac{E^-}{E^+} = \frac{Z_L - Z_0}{Z_L + Z_0} \tag{1.18}$$

where E^+ and E^- are the electric field strengths of incident and reflected wave, Z_L is the load impedance and Z_0 is the source impedance. The quality factor can also be determined experimentally from the reflection coefficient curve by measuring its *Full-Width at Half-Minimum* according to

$$Q = \frac{f_0}{FWHM} \tag{1.19}$$

From Equation 1.19, a narrower resonance signal corresponds to a higher quality factor of the device.

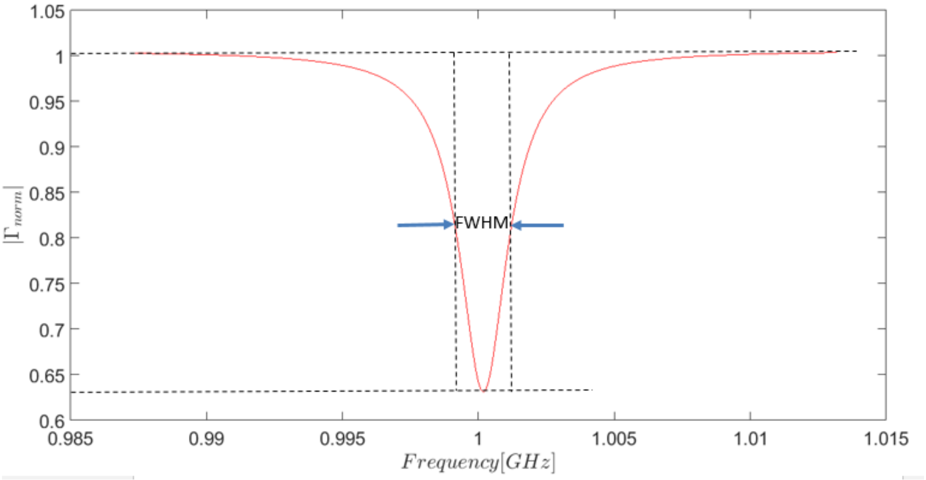

Figure 1.10: Quality factor measurement, showing a minimum at resonance.

As mentioned in section 1.4, a capacitor in the form of interdigitized fingers is used to achieve a good coupling from the input port to the main resonator structure. Microwave photons are injected into the resonator through this finger capacitance. The same structure is also used to probe the reflected signal which gives a measure of the quality factor of the resonator. There is also a possibility that the injected photons may leak out through this coupling capacitor attributing to the external losses. The coupling capacitor, the quality of the YBCO film and the dielectric losses can influence the total or the loaded quality factor (Q_L) of the resonator. When measuring the reflection coefficient [S11] of such a resonator, one obtains the loaded quality factor as

$$\frac{1}{Q_L} = \frac{1}{Q_0} + \frac{1}{Q_{ext}} \tag{1.20}$$

Here Q_{ext} is the quality factor which is a measure of the loss of the resonator caused by the outside world via the coupling capacitor, and Q_0 is the unloaded quality factor which represents the losses in the resonator itself. This intrinsic quality factor has different contributions.

$$\frac{1}{Q_0} = \frac{1}{Q_\epsilon} + \frac{1}{Q_{rad}} + \frac{1}{Q_\rho} \tag{1.21}$$

where, Q_ϵ, Q_{rad} and Q_ρ denote the quality factors associated with the dielectric, radiation and conductor losses of the resonator respectively. The dielectric losses are related to the $\tan\delta$[6] of the substrate. Radiation losses represents the leakage of energy from the microstrip line and can be minimised by carefully designing narrow conduction lines [25]. The conduction loss depends on the surface resistance of microwave transmission line and the ground plane.

The length of the coupling capacitor can be changed accordingly and it also determines if the resonator is over coupled, under coupled or critically coupled. When $Q_0 > Q_{ext}$, the losses in the resonator are mainly due to leakage in the coupling capacitor, and the resonator is said to be overcoupled. When $Q_0 < Q_{ext}$, the losses are from the material surface resistance, the dielectric and radiation; the resonator is undercoupled. The resonator is critically coupled and matched when $Q_0 = Q_{ext}$. A high quality factor can be obtained by reducing the coupling strength. However, it should not be reduced below a point where the resonator cannot be excited at all.

1.6 Microwave Properties of Superconductors

In this section, some important properties are emphasized by including superconductivity in the coplanar waveguide structure design. The microwave regime (1–100 GHz) corresponds to lower energy scale (1 GHz = 0.0041meV) and this is much lower than that of the superconducting energy gap. Measurements of the microwave response of a superconducting circuits have been used in recent years to determine conductivity in the HTS materials. Here, some properties which are important for including superconductivity in CPW resonators are discussed.

1.6.1 Kinetic inductance

The *two fluid model* proposed by Gorter and Casimir can be used to derive the complex conductivity of superconductors, which reveals many important behavioral properties [26]. This model postulates that a fraction of the conduction electrons are in the superconducting ground state (n_s) which do not undergo any kind of scattering, and the remaining electrons are in the normal excited state (n_n). The normal electrons or quasi particles are subjected to scattering and hence exhibits dissipation. The complex conductivity of a superconductor can be derived as $\sigma = \sigma_1 - i\sigma_2$. The real part of this conductivity gives information on the dissipation associated with quasiparticle excitation whereas the imaginary part can be used to determine the penetration depth.

Combining Drude's model with the two-fluid model, one obtains expressions for the real and imaginary part of the conductivity:

$$\begin{aligned}\sigma_1(\omega) &= \frac{n_n e^2 \tau}{m(1+\omega^2\tau^2)} \\ \sigma_2(\omega) &= \frac{n_s e^2}{m\omega} + \frac{n_n e^2(\omega\tau)^2}{m\omega(1+\omega^2\tau^2)}\end{aligned} \tag{1.22}$$

---

[6] $\tan\delta$ also known as the dissipation factor, is the tangent of the loss angle and Loss factor $L = \epsilon_r \tan\delta$.

where m is the mass of charge carriers, n_s is the superconducting carrier density, n_n is the normal electron density, ω is the electric field frequency and τ_i is the relaxation time (i=n,s). For frequencies below the energy gap, it can be assumed that frequencies are low enough such that $\omega\tau << 1$. Then the combined response of the two fluids reduces to:

$$\begin{aligned} \sigma_1(\omega) &= \frac{\pi n_s e^2}{2m}\delta(\omega) + \frac{n_n e^2 \tau_n}{m} \\ \sigma_2(\omega) &= \frac{n_s e^2}{m\omega} \end{aligned} \tag{1.23}$$

In Equation 1.23, the first term σ_1 corresponds to contributions from normal fluid which results in nonzero dissipation in superconductors at all nonzero frequencies. The reactive part σ_2 arises from the lossless motion of the Cooper pair neglecting the contributions from inertial effects of normal electrons. *Kinetic inductance* is the manifestation of the kinetic energy of the Cooper pairs.

In normal conductors, the collision time is very small ($\tau \approx 10^{-14}s$) and hence for frequencies around $100GHz$, can be ignored. Kinetic inductance is therefore only significant at higher frequencies and in superconductors where there is no scattering or $\tau \to \infty$. Kinetic inductance in superconductors is exploited to make efficient microwave propagation lines as it increases the inductance per unit length of superconducting transmission lines. When a signal is passed through the microwave strip lines, it absorbs photons modifying the Cooper pair density and consequently showing measurable changes in kinetic inductance. From the kinetic inductance measurements using co-planar waveguides, the london penetration depth and surface resistance of thin film superconductor can also be evaluated.

1.6.2 London penetration depth

As discussed earlier, the London penetration depth (λ_L) is one of the characteristic lengths which describes the exponential decay of magnetic field at the surface of a superconductor. This is in agreement with the experimentally observed Meissner effect, where the external magnetic field is effectively excluded from the bulk of superconductors. In case of anisotropic superconductors such as YBCO, London penetration depth is different along ab and c directions of transport. Therefore, the transport along any arbitraty direction is characterized by an effective london penetration depth expressed as [27]:

$$\lambda_{eff}^2 = \lambda_{ab}^2 \cos^2\theta + \frac{1}{2}(\lambda_c^2 + \lambda_{ab}^2)\sin^2\theta \tag{1.24}$$

From the two fluid model, the total number of conduction electrons is a constant $n_s + n_n$ but their ratio has a dependence on the temperature as,

$$\frac{n_s}{n} = 1 - \left(\frac{T}{T_c}\right)^n \tag{1.25}$$

The temperature dependence of n_s implies that λ_L also follows the same dependence on temperature.

$$\lambda_L(T) = \lambda_L(0)\left[1 - \left(\frac{T}{T_c}\right)^n\right]^{-\frac{1}{2}} \tag{1.26}$$

where $\lambda_L(0)$ is defined by

$$\lambda_L(0) = \sqrt{\frac{m}{\mu_o n q^2}} \tag{1.27}$$

and m,q and n are the mass, charge and volume density of superconducting carriers. $\lambda_L(0)$ strongly depends on the oxygen content of cuprates and can be determined from the critical temperature measurements. This indirectly indicates the presence of nodes in gap of the energy spectrum [3] associated with the condensation of the superconducting state. At 0K, superfluid density is changed by magnetic field and hence penetration depth also depends on magnetic field and this is very important to understand the mechanism of high-temperature superconductivity.

1.6.3 Surface resistance

The electromagnetic response of a conductor, whether superconducting or normal, can be represented by a complex surface impedance, $Z_s = R_s + iX_s$, where R_s is the surface resistance and X_s is the surface reactance. The surface resistance is the square resistance of the surface layer of thickness equal to the skin-depth, the distance within the electromagnetic field penetrates in a metal. The surface resistance of normal conductor has a frequency dependence of $f^{0.5}$, as compared to a superconductor which has a f^2 dependence. Hence, superconductors have lower surface resistance than normal conductors by three orders of magnitude at microwave frequencies which make it perfect candidates for many microwave circuit applications. The surface resistance of HTS at microwave frequencies is responsible for the loss in planar transmission lines and also for the decay of oscillation in resonators, and hence deteriorates the quality factor of the device.

Even though resistive losses in superconductors are much lesser than in normal metals, it cannot be neglected. The surface resistance (R_s) for a particular device geometry tells us about the resistive losses and the reactive impedance (X_s) controls the performance of the device. If the thickness of the sample 'd' is comparable to λ_L, then surface impedance is reduced to a simple expression [28]. The final expression for a thin film, after simplifying and applying transformation to the above expression results in:

$$\begin{aligned} R_s(T) &= (\omega\mu_0)^2 \frac{\lambda_L^4(T)}{d} \sigma_n(T) \\ X_s(T) &= \omega\mu_0 \frac{\lambda_L^2(T)}{d} \end{aligned} \tag{1.28}$$

These equations are not valid as temperature T increases towards T_c, since λ_L starts to increase while the field penetrates completely. The surface resistance of a superconducting coplanar waveguide can be calculated from its quality factor and

London penetration values [28]. If the thickness of the superconducting film is lesser than the London penetration depth, the surface resistance is expressed as:

$$R_s = \frac{\mu_0 \omega_r L' \lambda_L}{Q_{int} L'_{kin}} \frac{\lambda_L}{t} \tag{1.29}$$

The kinetic inductance per unit length L'_{kin} is then calculated with

$$L'_{kin} = \mu_0 \frac{\lambda_L^2}{t} \frac{C'_1 + C'_2}{2s} \tag{1.30}$$

where C'_1 and C'_2 are parameters which depend on the geometry of the coplanar waveguide transmission line [28].

1.7 Temperature dependence

The temperature dependence of microwave absorption in superconductors offers a distinct method to study high kinetic inductance and quality factors in HTS. The behaviour of these parameters at higher temperatures have been quiet straight forward and can be explained in terms of the change in the complex microwave surface impedance associated with quasiparticles. As the temperature is reduced, the number of thermally excited quasiparticles also decreases, thereby improving the quality factor (less dissipation).

The behaviour of resonators in the milli-kelvin temperature regime is quiet different. It is observed that quality factor of the resonator improves by increasing temperatures to around 1.5K. This behaviour has been observed in many groups [3][29]. For conventional superconductors, the most widely accepted explanation is that losses at milli-kelvin temperatures are unrelated to dissipation mechanisms in superconductor, but they are influenced by the saturated Two-level System (TLS) which usually materializes in the substrate [30]. The TLS are considered to be microscopic in nature originating due to lattice imperfections [31]. They disrupt the operation of resonator by coupling their electric dipole with the electromagnetic field in the resonator. The bath of TLS with energy splitting around hf_0 becomes thermally saturated for temperatures $T > \frac{hf_0}{k_B}$. Experiments have also confirmed that TLS absorbs energy in the low power, low temperature regime [3]. Earlier studies have focused on the evaluation of losses in silicon and germanium substrates, but with the development of many superconducting devices, state-of art lithography techniques and new dielectrics, it has become necessary to evaluate the loss mechanism in new substrate materials.

As seen in earlier Equation 1.21, there are different mechanisms which contributes towards the unloaded quality factor of the resonator. In the low temperature and low-power regime, dielectric losses in particular are said to be associated with resonant absorption due to the presence of a TLS system. The resonant interaction of TLSs with the microwave electric fields leads to a temperature and power dependent variation of the dielectric losses. The dielectric loss, $\tan\delta_{res}$ can be derived as [32]:

$$\tan\delta_{res}(T,P) = F\alpha_{TLS}\left[1+\frac{P}{P_c}\right]^{-\frac{1}{2}}\tanh\left(\frac{hf_0}{2k_BT}\right) \tag{1.31}$$

where $\alpha_{TLS} = \frac{\pi N d^2}{3\epsilon}$. F is the filling factor which depends on the geometry of the resonator and the electric field distribution in the strip lines, N is density of states in the TLS, $\epsilon = \epsilon_0\epsilon_r$ is the absolute permittivity of the dielectric with ϵ_0, the vacuum permittivity and P_c is the critical power which is fixed for each dielectric material. At a specific temperature, in the low-power limit i.e, if the probing signal power is maintained below a critical power P_c, $\tan\delta_{res}$ saturates to

$$\tan\delta_{res}(T) = F\alpha_{TLS}\tanh\left(\frac{hf_0}{2k_BT}\right) \tag{1.32}$$

In the high-power probing context, the dielectric losses decreases as $P^{-\frac{1}{2}}$. The unloaded microwave losses (Q_0) in the low-power regime can be expressed as

$$\frac{1}{Q_0(T)} = F\alpha_{TLS}\tanh\left(\frac{hf_0}{2k_BT}\right) + \frac{1}{Q_b} \tag{1.33}$$

where $\frac{1}{Q_b}$ is the background term which has the lossy contributions from conductor, radiation and other complex loss mechanisms, which is treated as a constant in this specific setup. In this low temperature range, both the geometric inductance and kinetic inductance are treated as a constant.

By applying the *Kramers-Kronig* mathematical relation to Equation 1.31, a correlation between the resonance frequency and temperature can be established [32] in the low power limit. Resonant absorption in the TLS also contributes to variation in the temperatures of the resonant frequency ($\delta f_0(T)$) and this can be expressed as

$$\delta f_0(T) = \frac{F\alpha_{TLS}}{\pi}\left[\ln\left(\frac{T}{T_0}\right) - [g(T,f_0) - g(T_0,f_0)]\right] \tag{1.34}$$

where, $\delta f_0(T) = \frac{f_0(T)-f_0(T_0)}{f_0(T_0)}$ and $g(T,f) = Re[\psi(\frac{1}{2} + \frac{hf}{2\pi i k_B T})]$ with ψ, the complex digamma function which is only significant for temperatures $T \leq \frac{hf_0}{2k_B}$. For a resonance frequency of around 5.45 GHz, it corresponds to $T \simeq 200mK$ which is set as the reference temperature T_0 in the above equation. Thus, resonance frequency shifts are observed which is mainly influenced by the temperature dependent dielectric constant.

1.8 Magnetic field dependence

A superconducting CPW resonator with sufficiently high quality factor is very sensitive to low magnetic fields and this feature can be exploited in various applications like sensitive magnetometers [33], kinetic inductance detectors [34] and parametric amplifiers [35]. Meservey and Tedrow [36] had first observed the variation of kinetic inductance of superconducting thin films under the influence of an external magnetic field. Most of these devices are based on the variation of the kinetic inductance as a function of current flowing through the superconductor.

One of the parameters which characterizes the magnetic flux penetration in a superconducting film is the distribution of screening current(J_s). This is essential for designing any non-linear device. In a superconducting loop composed of thin film with thickness h and width w, when $h << \lambda_L$, the circulating current density J_s can be considered as homogeneous within the cross-section of the thin film.

$$I_s = J_s wh \tag{1.35}$$

When an external magnetic field is applied perpendicular to the loop, constant circulating currents are formed which is a state of dissipationless flow of paired electrons. Consequently, it generates a magnetic field of its own. This field tries to oppose the external applied field and neutralises any flux inside the superconducting film. The magnetic flux quantization through the loop is given by:

$$(L_k + L_g)I_s - \Phi_a = m\Phi_0 \tag{1.36}$$

where I_s[A] is the screening current, Φ_a [Wb] is the applied magnetic flux, m is an integer and $\Phi_a = 2.07fWb$, the flux quantum. L_k and L_g are the kinetic and geometric inductances respectively. The kinetic inductance (L_k) per unit length arises from the kinetic energy (E_k) stored in the motion of the charge carriers (Cooper pair) and the magnetic (geometric) inductance (L_g) is a result of the energy stored in the magnetic field of the inductor. In the nanometre scale, L_k scales with the length of wire and inversely with the cross-sectional area and is given by

$$L_k = \frac{\mu_0 \lambda^2 l}{wh} \tag{1.37}$$

So for a superconducting film, L_k can be very large and dominate the Lg component (zero dc resistance) of the inductance at GHz frequencies.

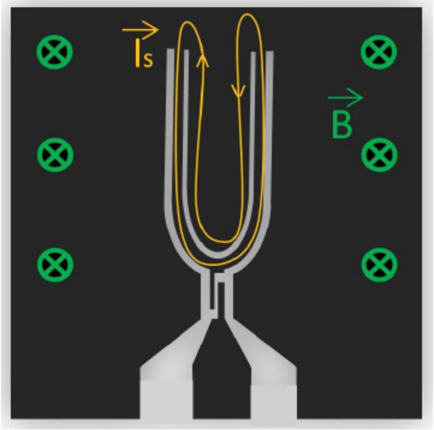

Figure 1.11: Screening current in a CPW resonator.

On increasing the external magnetic field, the supercurrents also increase reaching a maximum critical value. This shielding current increases the kinetic energy of the superconducting electrons and modifies the L_k of the resonator. At this point, any small excess current will cause the Cooper pairs to break down and reduce their density. The reduction of the Cooper pair density will increase the london penetration depth causing the kinetic inductance to increase. For a thin film with thickness small compared to the London penetration depth, which has no vortices entering the edge of the film and whose temperature is close to Tc; the first London equation and calculations from the Ginzburg-Landau theory result in [37]:

$$L_k = \frac{\mu_0 \lambda^2}{\rho} \left(1 - \frac{v_s^2}{v_m^2}\right)^{-1} \tag{1.38}$$

where μ_0 is the permeability constant, λ [m] is the London penetration depth, ρ [m2] is the cross-section area, v_m [m/s] is the velocity at which the Cooper pairs start to break up and v_s [m/s] is the velocity of the superconducting electrons. With sufficiently small I_s, the following approximation can be made $\frac{V_s}{V_m} = \frac{2I}{3I_c}$ [37]. Rewriting Equation 1.38, one gets:

$$L_k = L_0 \left(1 + \left(\frac{I_s}{I^*}\right)^2\right) \tag{1.39}$$

where L_0 is the kinetic inductance at zero screening current and I^* is a parameter, which is in the order of the critical current. At this point the sample is completely penetrated by the magnetic flux. Any small changes in the kinetic inductance can easily be measured by monitoring shift in resonant frequency of the CPW resonator according to Equation 1.15. Hence, by studying the behaviour of superconductors in magnetic fields, the principal magnetic properties of the material can be surveyed.

2

Experimental techniques

This section reviews the various micro-fabrication processes and measurement setup techniques involved in the characterization of the (103)-YBCO CPW resonators. All the resonators were fabricated in the clean-room facility at *Nanofabrication laboratory - MC2, Chalmers* which focuses on research in areas of nano and quantum devices. Before starting with the fabrication, photolithographic (positive) masks were made using lift off process.

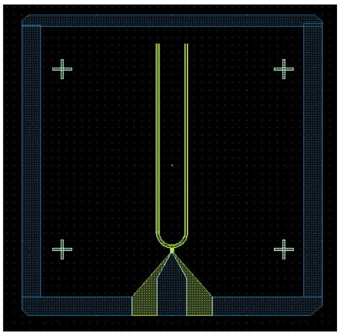

Figure 2.1: Mask layout of the CPW resonator design

2.1 Fabrication of CPW resonator

A CPW resonator is patterned on a (103) oriented YBCO thin film deposited on a dielectric substrate. A bonding pad structure in the form of a gold frame is used to contact the device to the measurement setup. The following steps describe the fabrication of the gold frame as well as the main resonator device.

2.1.1 Substrate choice

To obtain a high quality of (103) oriented YBCO thin film, the substrate has to be chosen carefully, such that the lattice constants must match with that of the superconductor and there must be no chemical reaction between these two materials. A transparent ceramic oxide, lanthanum aluminate strontium aluminium tantalate (LSAT), which has the chemical formula $(LaAlO_3)_{0.3}(Sr_2TaAlO_6)_{0.7}$ was used as a substrate for the epitaxial growth of (103)- oriented YBCO. The surface of the substrate has a 3.5° vicinal cut in order to initiate a single growth orientation of the (103) YBCO.

LSAT was preferred over other substrates like MgO and $LaAlO_3$ (LAO) since LSAT is characterized by low dielectric constant ($\epsilon \approx 23$) and low losses ($\tan\delta \approx 1 * 10^4$) at room temperature. It also combines the good microwave properties of LAO with the structural stability of STO [38]. Unlike LAO substrate, it has no twinning, no strain and is distinguished by its isotropic microwave properties [39]. Moreover, recent results [3] also showed that it has a very low value for the intrinsic dielectric losses ($F\alpha_{TLS} = 3 * 10^5$) in the low temperature and low power limit. Its matching structural lattice parameters with high melting temperatures and low electrical conductivity make it a feasible candidate as a microwave dielectric substrate for the realization of HTS based CPW resonator device.

Substrate cleaning

Before starting with any fabrication process, the 5x5 mm^2 LSAT substrate is washed and cleaned to remove any dust particles. First, it is immersed in warm acetone solvent at 50 °C followed by an ultrasonic bath for 5 minutes. The substrate is then carefully cleaned with a cotton tip in an isopropyl (IPA) bath and dried with a jet of N_2 air. It is also checked for dust particles remnants by optical microscope investigation.

2.1.2 Epitaxial (103)-YBCO film deposition

To obtain high a high quality $YBa_2Cu_3O_7$ thin film, there should be a relatively low strain between the LSAT substrate and material. High quality (103) oriented YBCO thin films can be obtained by pulsed laser deposition (PLD) system from stoichiometric pellet targets. The PLD technique maintains the stoichiometry of the target and offers a controllable YBCO epitaxial growth, which can be tuned by several parameters, such as the energy and repetition rate of the laser pulse, the temperature and the partial pressure of oxygen flow in the chamber.

Sample preparation using pulsed laser deposition

In most of the HTS film growing techniques, the structure of the film changes during the growth process. The stiochiometry of YBCO being deposited has to be maintained close to the correct composition as possible and this required post annealing at higher temperatures. But the higher temperature causes irregular growth of YBCO at the film-substrate interface[1] rendering them unsuitable for microwave applications. To prevent this problem, a two step process involving an insitu annealing procedure which allows the growth of the film at lower temperature is used to grow epitaxial films using pulsed laser deposition (PLD) ablation technique.

The YBCO thin film was deposited using a PLD system built at Chalmers, named CALAS. Approximately 120 nm of (103) YBCO was deposited at a rate roughly about 40 nm/min. In CALAS system, the substrate is glued to the steel plate stage using silver glue which causes heat transfer from heater to substrate by contact. The plate was heated using a resistive heater. The chamber was then evacuated to $3 * 10^{-6} mbar$ to remove all the water vapour and dust particles. The

---

[1] Change of the structure during the process is related to the initial stage of nucleation of HTS nuclei at the substrate-film interface

YBCO film is then deposited (maintaining oxygen pressure at 0.6*mbar*) in two steps maintained at different temperatures to promote good epitaxial growth: first layer is grown at 750 °C involving 400 pulses, followed by 2200 pulses at 800 °C.

After deposition, the temperature is lowered to room temperature at a rate of 10 °C/*min* and the oxygen pressure is increased to 650*torr*. This post annealing oxidation is a critical process considering that it affects the required stoichiometry of oxygen atoms in the deposited film and can change the critical temperature and other properties significantly.

To investigate the quality of the thin film, validate certain fabrication process steps and to examine the achieved resonator design, several characterization techniques were used. An overview of these techniques is found in Appendix A.

Gold deposition using sputter deposition

After the PLD, approximately a 200 nm gold layer was deposited on the YBCO layer by sputtering technique. The gold layer served both as a protective layer for the YBCO (to prevent it from absorbing or releasing any oxygen or impurities) and as a starting material for the gold frame. The gold was deposited at room temperature with a deposition rate of roughly 1 nm/s.

2.1.3 Patterning resonator with optical photolithography and ion beam milling.

Figure 2.4 shows the main steps to pattern the bonding frame. First, the photoresist layer (S1813) is exposed to deep UV light through the chromium mask. After the development process (in MF319 solution), the resist areas which was not exposed, remain intact and act as a mask for the gold, which is later etched by Argon ions milling process.

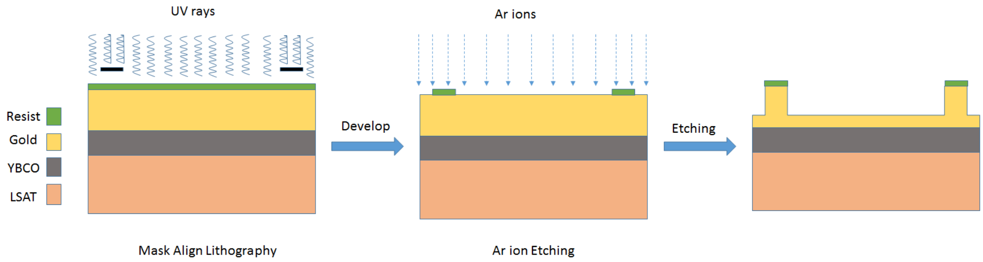

Figure 2.2: The process steps involved to create the gold frame.

The resonator structure shown in Figure 1.11 was then patterned using a second mask shown in Figure 2.1. Similar to the earlier procedure, a photosensitive polymer S1813 was whirled on the sample, baked and exposed to UV light using a mask aligner. At this step the coarse structures of the resonator is clearly visible by eye. In case of an undesirable design, the substrate can be cleaned, spincoated and exposed again. Proper development and clean surface was confirmed by optical microscopy.

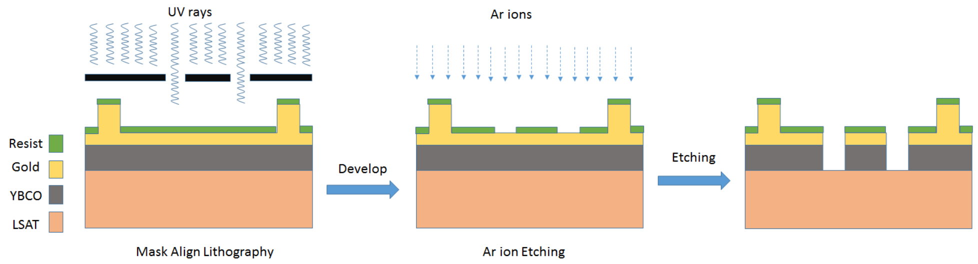

Figure 2.3: The process steps involved in making the resonator design.

The micro-gaps were further etched using a Ar-ion beam milling system (OXFORD instruments) by firing charged ions at the surface at an angle of 5 °. Also, the sample was etched longer to ensure that all the YBCO was removed in the desired areas (the gaps) [2]. The unexposed photoresist is also removed using soft ashing process such as oxygen plasma etching, since the ion beam milling would have harden the resist which makes it difficult to dissolve in acetone.

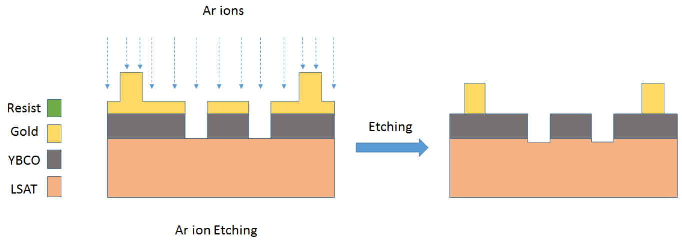

Figure 2.4: The final processs step

Finally, to remove the last 50 nm of protective gold layer covering the exposed areas of the resonator design, argon ion etching was used again. The presence of the gold, in fact, could degrade the surface resistance of the YBCO film, resulting in worse performances of the final device.

During the development of the resonator design, it was observed that the edges in the resist were a bit rough and that the gaps in the resonator design were a bit too wide. The roughness was due to the inability to use hard contact mode during the photolithography, because of the uneven substrate (caused by the silver glue). The increased width of the gaps was due to over-development. To improve the fabrication, a laser writer[3] (Laser writer DWL 2000) could be used instead of the mask aligner for better resolution of the feature size.

---

[2] A secondary ion mass spectrometer (SIMS) was used during this etching step, see Appendix A for further description.

[3] Which uses direct writing technique without hard contact mode.

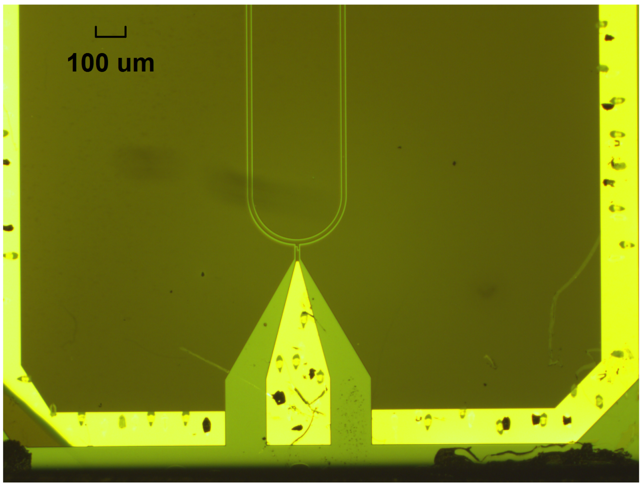

Figure 2.5: Optical image of the final device.

Wire bonding the resonator

The sample is usually mounted inside a closed sample holder which provides connection to the coaxial cables. Aluminium wire bonds were used to connect the YBCO in-out pad structure and gold frame to the sample holder. For a good ground connection, many wires are bonded on the gold frame. Now the resonator device is ready for testing and mounted into the measurement setup.

2.2 High frequency measurement setup

To fully characterize the CPW resonator in single photon limit, a carefully designed measurement setup is assembled. This involves an integrated system of microwave instruments, devices and dilution refrigerators.

2.2.1 Measurement procedure

The measurements are done by sending photons of different frequencies from a RF generator to the resonator, via the coupling finger capacitor. The amplitude of the reflection coefficient ($\Gamma = Vout/Vin$) is measured with a Vector network analyzer (VNA) and the data is analysed. Since the measurements were to be made at low temperature, the sample was cooled down to $20mK$ and maintained at this temperature for specific measurements. The low temperature range is of interest, since it corresponds to a low number of photons, where higher temperature would produce a continuous spectrum of photons.

To achieve such low temperatures, an Oxford Triton dilution based refrigerator was used. It offers an electrically shielded environment with ultra-low vibration and milli-kelvin temperatures suitable for performing sensitive experiments. The sample holder was shielded with $\mu - metal$ to prevent any interference by ambient magnetic field.

A schematic of the experimental setup used for RF characterization measurements is shown in Figure 2.6. The experimental setup consists of different stages, each maintained at different temperatures ranging from 60K to 20mK. The sample holder is thermally anchored to the mixing chamber plate which is maintained at 20mK. Since only few photons are desired in these measurements, the power of incoming signal is reduced by appropriate attenuators positioned at different temperature stages, see Figure 2.6. Two circulators are also mounted in series. The circulators redirect the photons reflected from resonator to the output path. Moreover, they are used in order to prevent any thermal noise signal arising from the low noise amplifier (LNA) from entering into the resonator device. Each circulator, in fact, provides an attenuation of -35 dB to the noise signal, before it reaches the resonator. The reflected signal from the circulators is then passed through a band-pass filter in order to remove any unwanted noise, and is finally amplified and read out using a VNA.

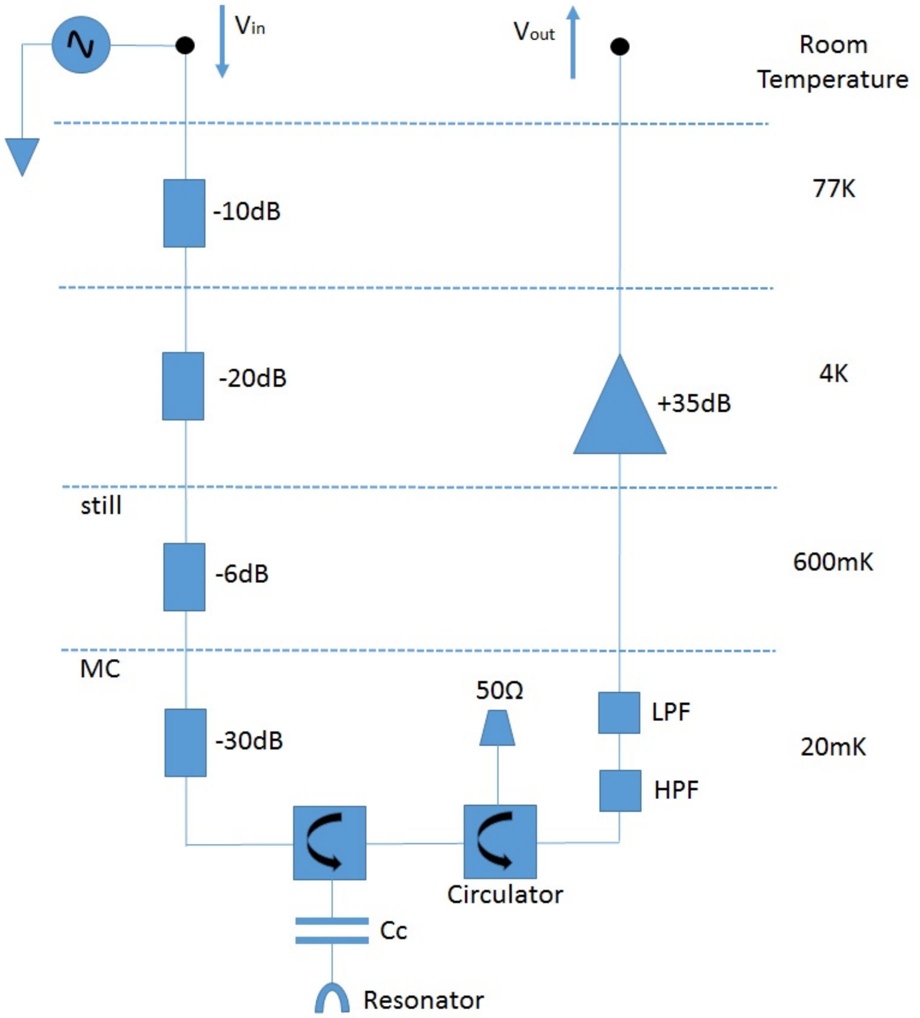

Figure 2.6: Schematic of the microwave setup for single photon characterization measurements.

3

Results and discussions

In this chapter, the measurement results are presented and discussed. The superconducting CPW resonator fabricated on LSAT using the CALAS system is characterized to find the various loss mechanisms. The film thickness is about 120nm and the X-ray diffraction results also show that it is all (103)- oriented YBCO without traces of c-axis growth. The resonator is mounted on the MC plate of the dilution refrigerator and their microwave response is measured by sweeping the frequency and adjusting the readout power of the VNA. For all the evaluations, only the fundamental frequency of the resonator is considered.

The chapter begins by listing the observation of reflection coefficient which displays a working resonator. Further, this section analyzes the measurement results of both the temperature and magnetic field dependence of the resonance frequency and quality factor. The extracted parametric values are then compared with that of the theoretical predictions which sheds some light on the dissipation mechanisms.

3.1 Reflection coefficient measurement

The raw data of the measurements was obtained as the amplitude of the reflection coefficient for different frequency values. A VNA was used to measure the complex S_{11} parameter. The amplitude of the reflection coefficient is plotted against the normalized frequency and a minimum was observed at the resonance frequency.

As can be seen in Figure 3.1, the reflection spectrum clearly displays a dip of width δf centered at the resonance frequency f_0. The data was normalised before the final plotting i.e., the amplitude of the reflection coefficient was normalised to the background signal and the frequency was normalised to the resonance frequency of the resonator.

The experimental data was also fitted with the complex valued reflection signal around f_0 given by the expression:

$$\Gamma = \frac{Q_{ext}^{-1} - Q_0^{-1} - 2i\delta x}{Q_{ext}^{-1} + Q_0^{-1} + 2i\delta x} \tag{3.1}$$

where Q_{ext}^{-1} is the external losses due to the coupling capacitor, Q_0^{-1} is the internal losses and $\delta x = \frac{f-f_0}{f_0}$ [3]. It is noted that the fitted curve matches the data rather well. The average number of readings when increased, gave a flat background value. The quality factors and fundamental resonance frequency f_0 can be extracted from this fit expression.

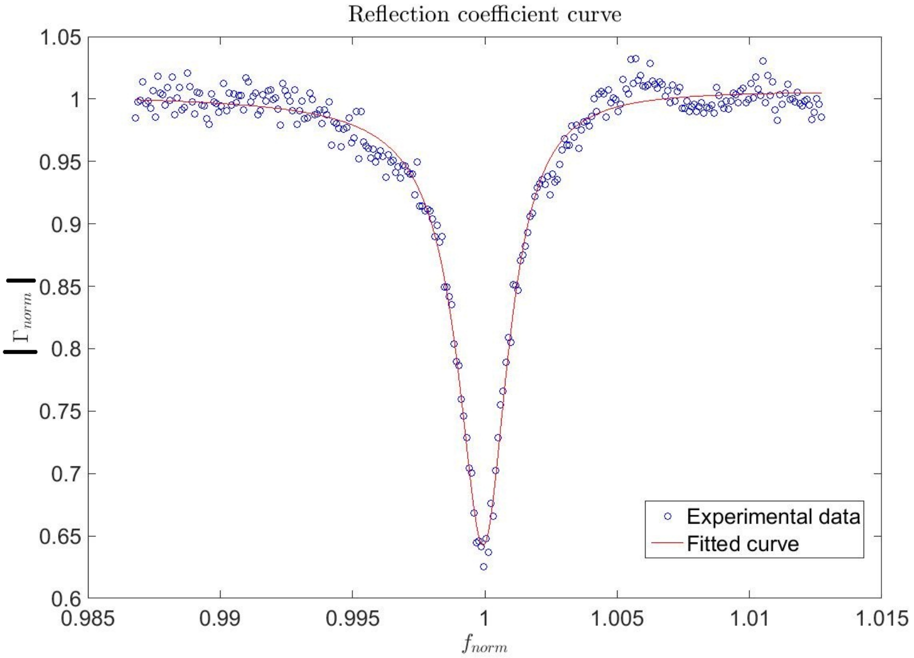

Figure 3.1: Normalised values of the reflection coefficient amplitude plotted against normalised frequency values. A minimum is observed at the resonance frequency.

3.2 Temperature dependence of microwave losses

Here, measurements of the temperature dependence of the internal losses in a (103) YBCO resonator is reported by studying the resonance frequency as a function of temperature in the low power limit. The sample holder carrying the resonator was thermally anchored at the mixing chamber (MC) of a dilution refrigerator whose temperature was varied from 18mK to 10K. Reflection data from the resonator were collected from the VNA. The input power of the microwave signal was fixed at -106dBm. The loss mechanism in superconducting resonators at low temperatures are partly governed by the dielectric losses. The temperature dependence of the resonance frequency is illustrated in Figures 3.2 and 3.3. Measurements under different conditions, i.e, with and without applying external field are compared.

The temperature dependence of the resonance frequency shifts is observed by slowly enhancing the system temperature, from 20 mK to 10000 mK. In the lower temperature range i.e., around 20mK, the frequency dependence from superconducting film should be rather constant. Any frequency changes observed can be attributed to the dielectrics. Phenomenally, these behaviors can be explained in the framework of the Two level systems (TLS) theory where the resonant absorption due to TLS is believed to be a significant loss mechanism. By fitting the experimental data to Equations 1.21 and 1.34, the value of $F\alpha_{TLS}$ parameter (related to the dielectric losses) and background losses ($1/Q_b$) is extracted. The value of $F\alpha_{TLS} = 1.4 * 10^{-3}$ does not match with the values measured for LSAT earlier ($F\alpha_{TLS} = 3.4 * 10^{-5}$) [3] and the fit is quiet bad. One possible reason is that losses are from the conductor and most probably related to the vortices.

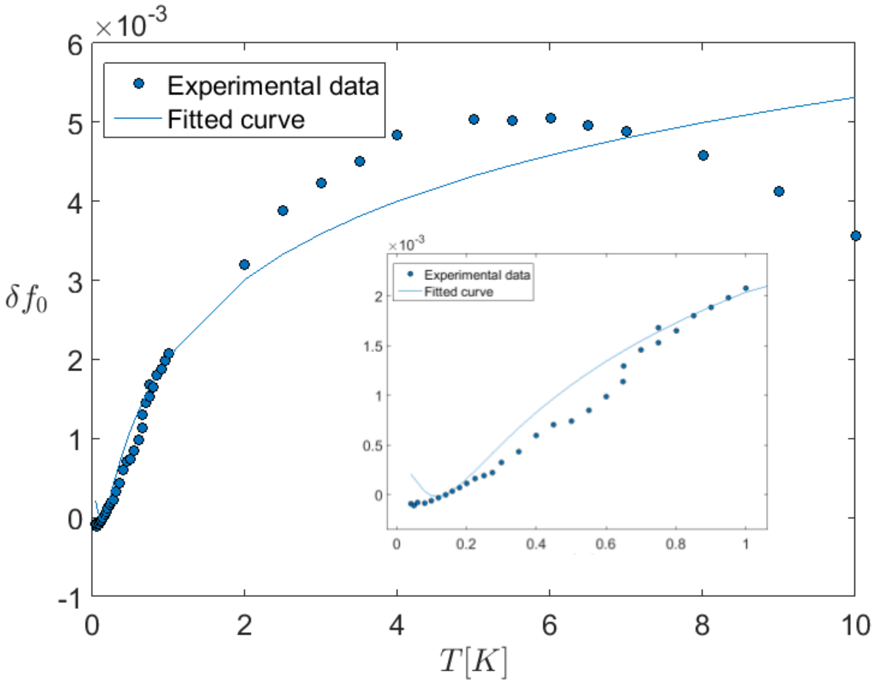

Figure 3.2: The resonance frequency variation plotted as a function of temperature at zero magnetic field for readout powers of -106 dBm. Inset : stretched representation of the same at low temperatures.

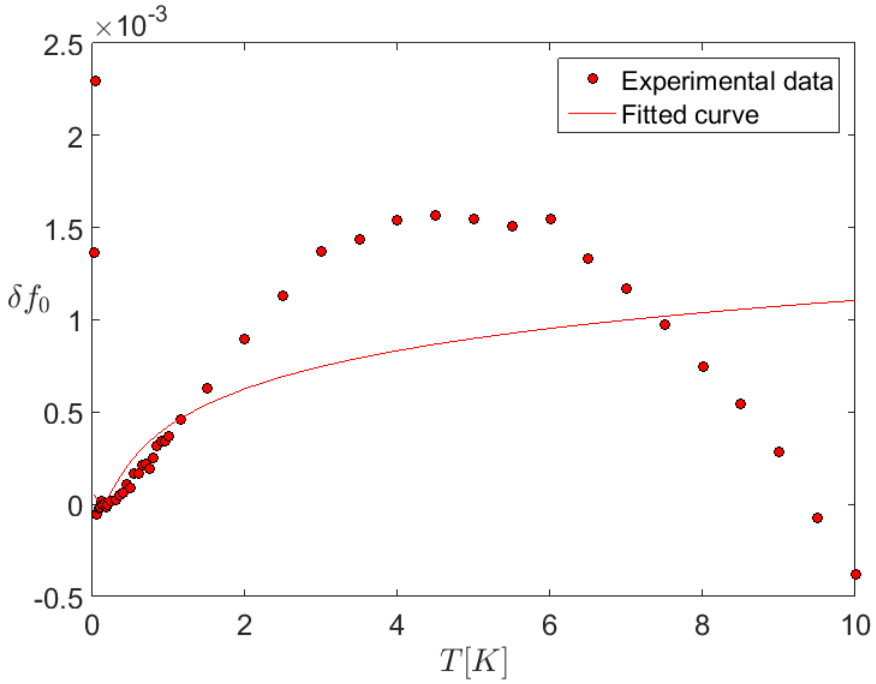

Figure 3.3: The resonance frequency variation plotted as a function of temperature measured at finite field. The solid line represents the best fit to Equation 1.34.

The resonance frequency was also measured by sweeping temperature in the millikelvin range from 20mK to 10000mK keeping the magnetic field at a point which corresponds to highest quality factor. This is shown in Figure 3.3. In this case too, the experimental values doesn't seem to correlate with the fit. For this resonator, the maximum variation in relative frequency δf_0 is way larger ($\approx 4*10^{-3}$) than that observed in any dielectric. The fitting parameter does not really fit the experimental values.

Comparing the two cases, with field and without field, the two temperature dependencies are completely different. This implies that the losses observed has nothing related to dielectric, and it is from the conductor which is mostly vortex related. It is still unknown why such a strong temperature dependency is observed and needs to be investigated. But it appears that strong pinning sites and rearrangement of vortices can be attributed to this temperature dependency.

The internal quality factor was further extracted from the reflection coefficient curves, and plotted as a function of temperature as seen in Figures 3.4 and 3.5. The losses ($1/Q_0$) are expected to decrease with increasing temperature in accordance with the TLS model.

However, (103) YBCO is more lossy, as its surface resistance is much larger compared to (001) YBCO. It is so large that we do not see the effects of dielectric, which is way lower. In this device, the quality factor is around 1000, (loss=10^{-3}), and it is very difficult to see the effects of the dielectric, since it will be overshadowed by that of YBCO. But maybe it is less strong because of the stray field, showing a weird field dependence implying that losses are not just because of conductor and dielectric. TLS is usually located at the interface, but with (103) YBCO and dielectric interface it appears to be conflicting giving rise to different values.

Again, the quality factor, with and without external fields look completely different. This asserts the claim that the losses observed are most probably because of the vortices. The experimental data also does not fit with the model explained by Equation 1.33. The extracted parameteric values of $F\alpha_{TLS}$ does not tell much about the intrinstic losses. The dielectric loss contribution cannot be resolved since it is not as large as other loss mechanisms. The total losses are given by $1/Q_{conductor} + 1/Q_{dielectrics} + 1/Q_{vortices}$, and the dominating part is the loss mechanism stemming from rearrangement of vortices. The rest of the loss mechanism are hidden and cannot be resolved.

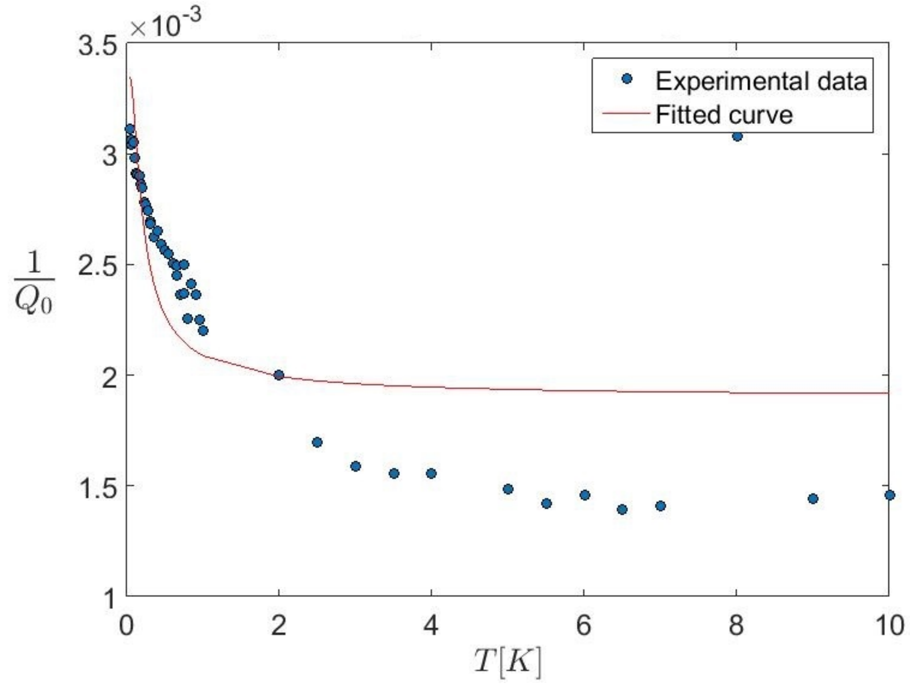

Figure 3.4: Internal quality factor curve vs. temperature. The solid line represents the fit to Equation 1.33.

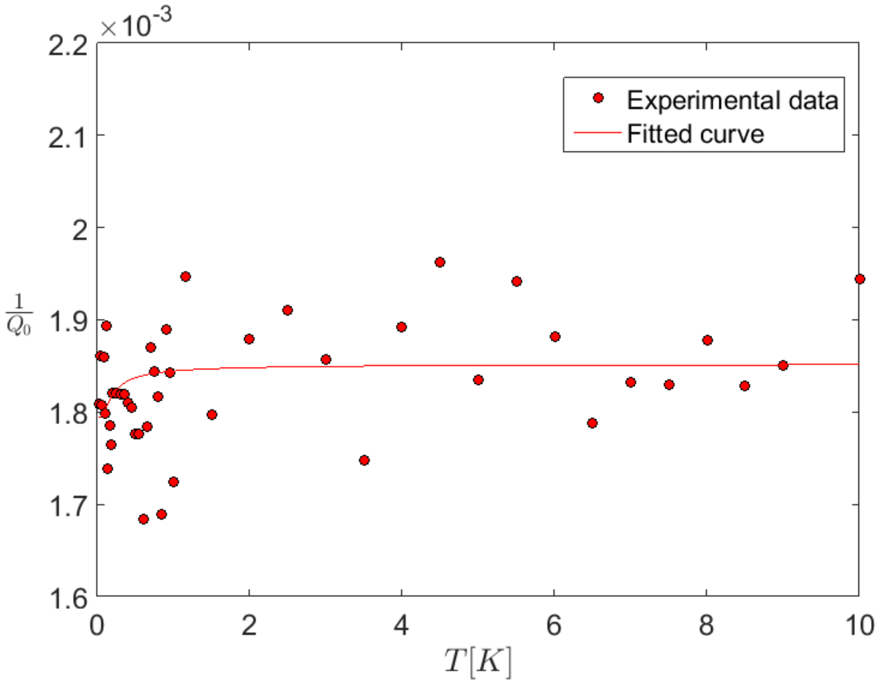

Figure 3.5: Quality factor curve vs. temperature in the presence of external field.

3.3 Magnetic field dependence

The external magnetic field is applied perpendicular to the sample by sending DC current through a copper stabilized superconducting solenoid, with a calibration factor of roughly $50\mu T/mA$, which is mounted on top of the sample holder.

As the applied field B_0 is adjusted between zero and a maximum value (0.25 mT), the resonance dip f_0 shifts towards a lower value as can be seen in Figure 3.6. The growing screening currents will cause the Cooper pair density to decrease, thereby enhancing the total inductance (refer Equation 1.39). This is seen in the form of resonance frequency shift Δf_0 towards lower values.

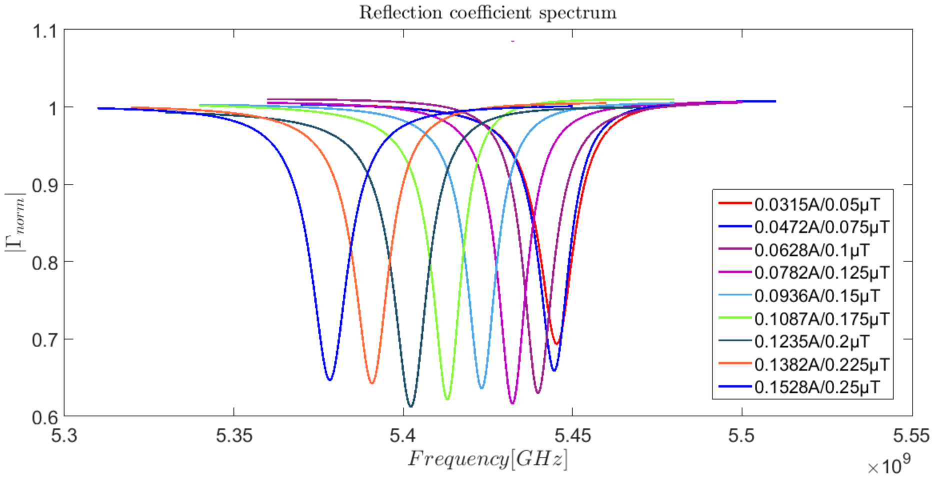

Figure 3.6: Resonator reflection coefficient measured as a function of applied external magnetic field.

The magnetic field is also applied by reversing the coil currents and measuring the reflection parameter. A small hysteresis behavior of the resonance frequency was observed by repetitively cycling the coil currents between +5mA and -5mA suggesting some remnant fields. Such hysteresis is related to dissipation mechanism associated to vortex entry and pinning near the edges of thin films. These vortices might have accumulated during the cool down process where the sample was not properly shielded. Either the rearrangement of previously trapped vortices or changes in the number of trapped vortices will contribute to the effect.

Figure 3.1 shows one instance of the reflection coefficient measurement. Essentially, separate reflection coefficient graphs were obtained for different settings of the copper coil current (the magnetic field) and all graphs showed similar resonance behaviour. These different resonance frequency values were plotted against the screening currents corresponding to different fields. The screening currents are related to the coil current values by:

$$\begin{aligned} B &= 50 * 10^{-6} * I_{coil} \\ \Phi &= B * A_{eff} \\ \Phi &= (L_k + L_g) * I_{screen} \end{aligned} \tag{3.2}$$

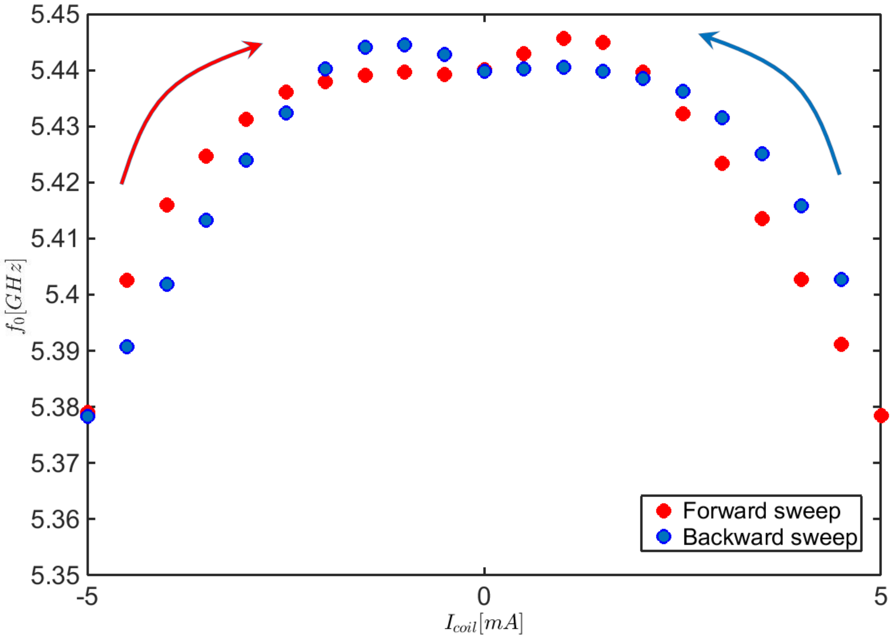

Figure 3.7: Hysteretical behavior of the resonance frequency as a function of an externally applied magnetic field.

where the constant in the above equation is a calibrated value for the coil current. A_{eff}, L_k and L_g are simulated values obtained from COMSOL. The resonance frequency, the kinetic inductance and the quality factor are plotted with respect to the screening current.

From Figure 3.8, it can be seen that the resonance frequency decreases as the screening current (or magnetic field) increases. It should be observed that the data close to zero field are omitted due to the strong hysteresis effects. It is further seen that the experimental data is explained well by the fitted curve, obtained from Equations 1.15 and 1.39. From this fit, the following parametric values were obtained, $L_{k0} = 1.12$ nH and $I^* = 444$ mA. The kinetic inductance at zero field is in the range of expected values, but the maximum screening current value I^* is much higher than the normal value.

The frequency was then converted to kinetic inductance, using Equations 1.15 and 1.39, to get data that corresponds to equation 1.39, which uses kinetic inductance and screening current as variables.

A kinetic inductance versus screening current graph is shown in Figure 3.9. It can be noted that the kinetic inductance increases with screening current and has a nonlinear dependence, as expected from Equation 1.39. It is again confirmed that the fitted curve, from Equation 1.39 using the same parameters as in Figure 3.9, matches the data well.

As a final step, information about the quality factor's dependence of the screening current is obtained from the reflection coefficient plots, such as Figure 3.10, and Equation 3.1.

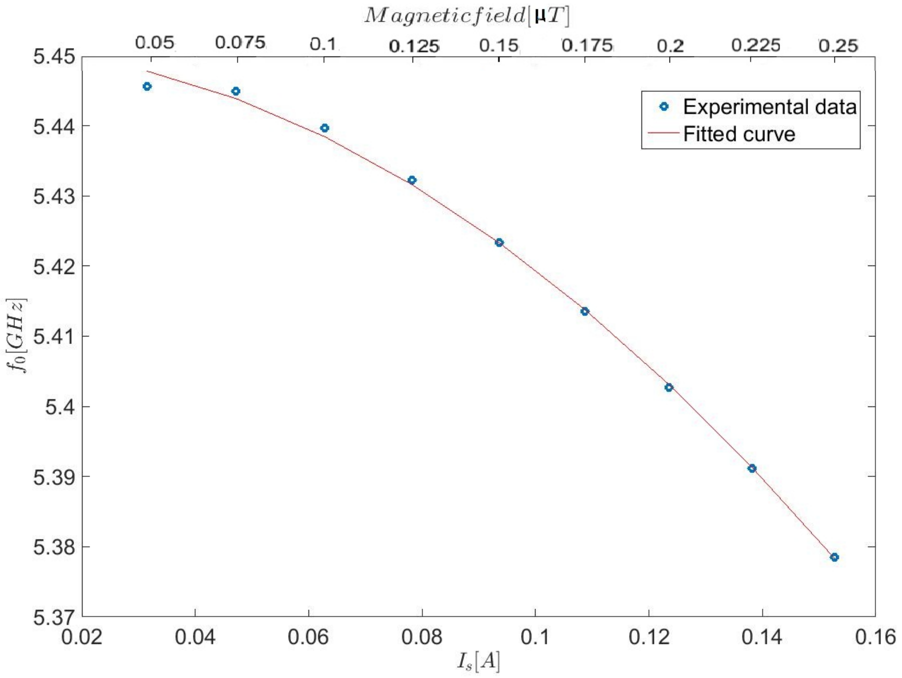

Figure 3.8: Resonance frequency values plotted against the corresponding screening current values.

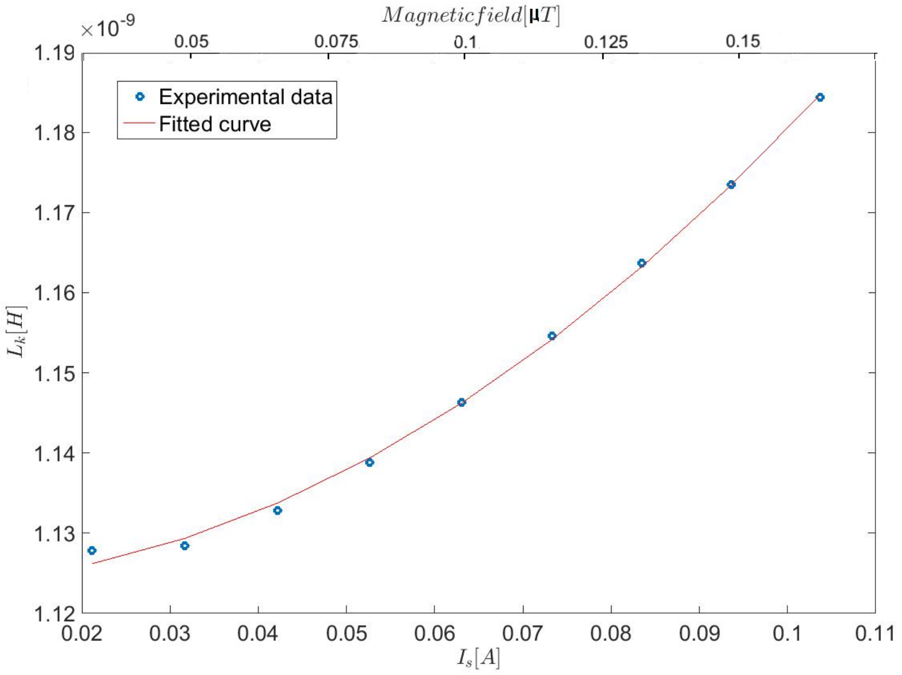

Figure 3.9: Kinetic inductance plotted against screening current.

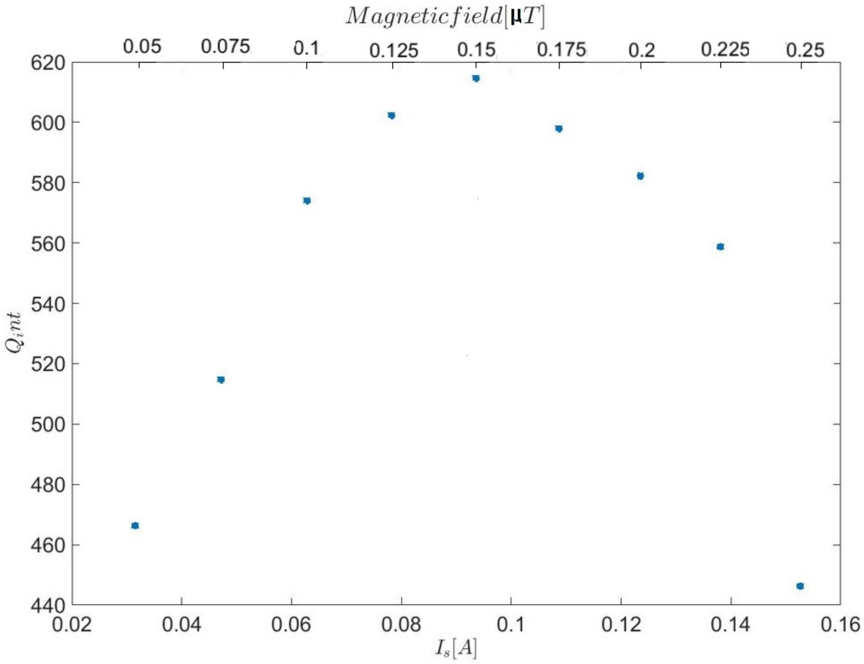

Figure 3.10: Quality factor plotted against screening current.

The quality factor is expected to behave similarly to the resonance frequency and is expected to decrease as the screening current increases. This is due to a reduction of Cooper pair density caused with an increase of conductor losses. However, Figure 3.10 shows an increase of the quality factor for screening currents ranging from 0.02 A to 0.06 A, before it starts decreasing.

This behaviour might be explained by vortices trapped in the edge of the film during the cool down process. Generally, AC currents are usually present on both central conductor strip and ground plane. The penetration of magnetic field changes the current distribution in the central conductor such that maximum current flows at the edges. These screening currents would exert Lorentz force on the vortices, rearranging and pushing them towards center of the film, resulting in increased dissipation, increasing the surface resistance and thereby lowering the quality factor. The quality factor gets larger at Q_{max}. At this point, the effect of the vortices is smallest. However, if the device has a stray internal magnetic fields, an external magnetic field could, to some extent, nullify the former, or vortices have been moved away from the region where large AC currents were present resulting in an increase of the quality factor.

3.4 Noise properties

In this section, the characterization of the responsivity and noise of the resonator device is presented which enables it to be used as a magnetometer. Noise is measured at a point, which has the largest response from the device and shows maximum sensitivity to external fields. But before that magnetic behavior is characterized. By differentiating Equation 1.36 and 1.39, the responsivity of the magnetometer is calculated from $\frac{\partial v_{out}}{\partial B_0}$, where v_{out} is the reflected voltage and B_0 is the applied magnetic field. At resonance, the responsivity can be approximated as[1]:

$$\begin{aligned} \left|\frac{\partial v_{out}}{\partial B_0}\right|_{f=f_0} &= \left|\frac{\partial v_{out}}{\partial L_{kin}} \frac{\partial L_{kin}}{\partial I_s} \frac{\partial I_s}{\partial B_0}\right|_{f=f_0} \\ \left|\frac{\partial v_{out}}{\partial B_0}\right|_{f=f_0} &= V_{in} Q \frac{I_s}{(I^*)^2} \frac{L_{kin,0}}{L_{tot}} A_{eff} \end{aligned} \tag{3.3}$$

where the resonator is excited with a voltage V_{in} and the resonator is considered at critical coupling ($Q_{ext} = Q_0 = Q$).The noise performance of the device was limited by the background noise of the electronics, so it might suggest that we cannot resolve the magnetic field noise of our device. In the above expression, certain improvements have to be made in order to get better responsivity. One way is to make larger effective area, increase the ratio $\frac{L_{kin,0}}{L_{tot}}$ or increase the quality factor. Also if the device is measured close to the critical current, it helps i.e., I_s is close to I^*.

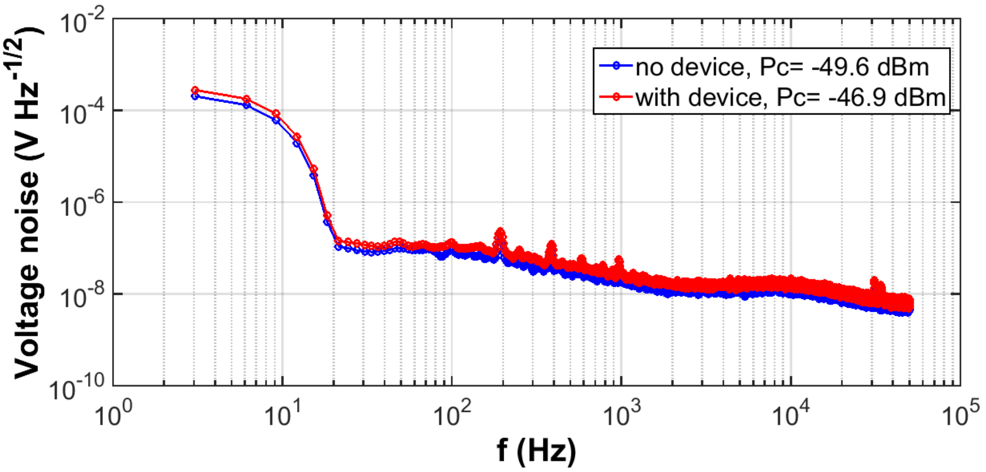

Figure 3.11: The measured spectral density of the equivalent voltage noise at high and zero field responsivity

There is no difference in the noise spectral density (Figure 3.11) with the device connected (the shift is due to the difference in power). This suggests that we cannot resolve the magnetic field noise of our device.

---

[1] Refer to Appendix C for more details

4

Conclusions and outlook

In the work described here, the fabrication and characterization of a superconducting coplanar waveguide resonator is evaluated. The temperature and field dependencies of the resonance frequency and quality factor were studied in the framework favourable to the transmon.

The temperature dependence of the resonance frequency and quality factor were compared to a model system of a bath of two level systems in the dielectric substrate. From the various observations, it can be inferred that dielectric losses cannot account for the change in frequency, since the shifts in frequency is way too high to be related to dielectric loss mechanism. The quality factor is also changing way too strongly to be associated with dielectric properties. The dependencies of quality factor with and without external fields also show conflicting data suggesting the loss mechanism from vortex rearrangement.

The likely possibility, points out that the device losses could have originated from vortex penetration during cool down process. This is the strongest reason for explaining temperature dependencies of resonance and quality factor of the CPW resonator. Since vortices exhibit their own internal fields at zero external magnetic fields, that can explain why there was an offset in the zero field-maximum frequency value. The circulating currents can push the vortex from edges towards the center of the central conductor. In order to prove such hypothesis, further investigations have to be made.

- A feasible control experiment would be to realize a resonator which would not contain any closed loops, e.g. a $\lambda/4$ resonator. Such a resonator would be much less sensitive to external magnetic fields due to the lack of "macroscopic" circulating currents. Moreover it would be also much less sensitive to the stray fields of trapped vortices.
- One can also perform detailed investigations in ultra low field cool down environment, obtaining the temperature curves without applying any fields. Active shielding have to be provided since it is difficult to cool down big films without vortices. If this too fails, then one can introduce nanostructure anti-dot arrays in superconducting films. At least, the vortices will be trapped and their movement will be hindered, making it possible to study the losses with a smaller contribution of vortex dynamics.
- Further goal is to perform field dependence measurements at high temperatures (7K-10K) and investigate if the hysteresis observed in the magnetic field dependence of the resonance frequency and quality factor of the resonator modify. Maybe, there is a threshold field below which the hysteresis curve vanishes. A similar temperature dependence on the threshold field was ob-

served, suggesting a relation between hysteresis and flux pinning [40].

For realizing a transmon using biepitaxial junctions of YBCO, a strong coupling regime is necessary. Under such a regime, one expects coherent interaction of superconducting artificial atom (qubit) with a single microwave photon. For this, a resonator with low internal losses are desirable. In the transmon design, the resonator is realised using (001) YBCO, whose losses are well withing the limit [3]. The zero field unloaded quality factor of (103) YBCO resonator measured at 20mK and low powers, which is around 400, should suffice for the realization of biepitaxial grain boundary josephson junctions. Such quantum circuits can be used as a powerful tool to probe the low energy quasi particle excitation spectrum in HTS which sheds more light on the origins of superconductivity in unconventional materials.

Some potentially promising results have been obtained as far as the fabrication of the device is concerned. In addition, the extra process steps that were involved to make the resonator has definitely harmed the superconductor's surface to some extent. Perhaps, the surface also deteriorated after being exposed to atmosphere. It is also important to understand the ill effects of process steps on the surface of YBCO. In order to be used for microwave applications, they must be able to survive the necessary processes involved. Considerable improvement in process fabrication and resonator designs can be made. One can also characterize (103)-YBCO resonator deposited on patterned CeO_2, in order to replicate the same fabrication steps involved in the biepitaxial growth of the transmon.

The frequency dependence of magnetic field is also of interest, since it confirms the nonlinear behaviour of HTS based resonator. Regarding its application as a magnetic field sensor, the noise properties or the sensitivity of the devices was tested and further work needs to be done to improve its performance. For magnetometer, the noise from the electronics overshoots the noise from the device, and hence one can improve various parameter to improve it.

Bibliography

[1] Saxena, Ajay Kumar. High-Temperature Superconductors. Vol. 125. Springer Science Business Media, 2012.

[2] Gustafsson, David, et al. "Fully gapped superconductivity in a nanometre-size $YBa_2Cu_3O_{7-\delta}$ island enhanced by a magnetic field." Nature nanotechnology 8.1 (2013): 25-30.

[3] Arzeo, Marco, Floriana Lombardi, and Thilo Bauch. "Microwave Losses in YBCO Coplanar Waveguide Resonators at Low Power and Millikelvin Range."Applied Superconductivity, IEEE Transactions on 25.3 (2015): 1-4.

[4] de Bruyn Ouboter, Rudolf. "Heike Kamerlingh Onnes's discovery of superconductivity." SCIENTIFIC AMERICAN-AMERICAN EDITION- 276 (1997): 98-103.

[5] Drozdov, A. P., et al. "Conventional superconductivity at 203 kelvin at high pressures in the sulfur hydride system." Nature (2015).

[6] Bednorz, J. George, and K. Alex Müller. "Possible highT c superconductivity in the Ba La Cu O system." Zeitschrift für Physik B Condensed Matter 64.2 (1986): 189-193.

[7] Wu, M., Ashburn, J., Torng, C., Hor, P., Meng, R., Gao, L., Huang, Z., Wang, Y. and Chu, C. (1987). Superconductivity at 93 K in a new mixed-phase Y-Ba-Cu-O compound system at ambient pressure. Phys. Rev. Lett., 58(9), pp.908-910.

[8] London, Fritz, and Heinz London. "The electromagnetic equations of the supraconductor." Proceedings of the Royal Society of London A: Mathematical, Physical and Engineering Sciences. Vol. 149. No. 866. The Royal Society, 1935.

[9] Landau, Lev Davidovich, and V. L. Ginzburg. "On the theory of superconductivity." Zh. Eksp. Teor. Fiz. 20 (1950): 1064.

[10] Gorelik, Leonid. Condensed Matter Physics 2014. Gothenburg: N.p., 2015. Print.

[11] Bardeen, John, Leon N. Cooper, and J. Robert Schrieffer. "Microscopic theory of superconductivity." Physical Review 106.1 (1957): 162.

[12] Giaever, Ivar, and Karl Megerle. "Study of superconductors by electron tunneling." Physical Review 122.4 (1961): 1101.

[13] Wollman, D., Van Harlingen, D., Giapintzakis, J. and Ginsberg, D. (1995). Evidence for $d_{x^2y^2}$ Pairing from the Magnetic Field Modulation of $YBa_2Cu_3O_7$ Pb Josephson Junctions. Phys. Rev. Lett., 74(5), pp.797-800.

[14] Van Harlingen, D. J. "Phase-sensitive tests of the symmetry of the pairing state in the high-temperature superconductors—evidence for $d_{x^2y^2}$ symmetry." Reviews of Modern Physics 67.2 (1995): 515.

[15] Bauch, Thilo, et al. "Macroscopic Quantum Tunneling in d-Wave $YBa_2Cu_3O_{7\delta}$ Josephson Junctions." Physical review letters 94.8 (2005): 087003.

[16] Carmi, R., et al. "Spontaneous macroscopic magnetization at the superconducting transition temperature of $YBa_2Cu_3O_{7-\delta}$." Nature 404.6780 (2000): 853-855.

[17] Bednorz, J. George, and K. Alex Müller. "Possible high T_c superconductivity in the BaLaCuO system." Zeitschrift für Physik B Condensed Matter 64.2 (1986): 189-193.

[18] Monthoux, P., A. V. Balatsky, and D. Pines. "Weak-coupling theory of high-temperature superconductivity in the antiferromagnetically correlated copper oxides." Physical Review B 46.22 (1992): 14803.

[19] Tsuei, C. C., and J. R. Kirtley. "Pairing symmetry in cuprate superconductors." Reviews of Modern Physics 72.4 (2000): 969.

[20] Äkäslompolo, Laura. 'Single Unit Cell Of YBCO | Department Of Applied Physics'. Physics.aalto.fi. N.p., 2015. Web. 30 Sept. 2015.

[21] Toulouse.lncmi.cnrs.fr,. 'Laboratoire National Des Champs Magnétiques Intenses-Toulouse-High-Tc Cuprates : Phase Diagram'. N.p., 2015. Web. 30 Sept. 2015.

[22] Wen, Cheng P. "Coplanar waveguide: A surface strip transmission line suitable for nonreciprocal gyromagnetic device applications." Microwave Theory and Techniques, IEEE Transactions on 17.12 (1969): 1087-1090.

[23] Gevorgian, Spartak, Peter LJ Linner, and Erik L. Kollberg. "CAD models for shielded multilayered CPW." IEEE Transactions on Microwave Theory Techniques 43 (1995): 772-779.

[24] Rauch, W., et al. "Microwave properties of $YBa_2Cu_3O_{7x}$ thin films studied with coplanar transmission line resonators." Journal of applied physics 73.4 (1993): 1866-1872.

[25] Sage, Jeremy M., et al. "Study of loss in superconducting coplanar waveguide resonators." Journal of Applied Physics 109.6 (2011): 063915.

[26] C. J. Gorter, H. B. G. Casimir: On supraconductivity I. Physica 1, 306–320 (1934)

[27] J. Johansson, K. Cedergren, T. Bauch, and F. Lombardi. Properties of inductance and magnetic penetration depth in (103)-oriented yba2cu3o7 thin lms. Phys. Rev. B, 79(21):214513, Jun 2009.

[28] Vendik, Orest G., Irina B. Vendik, and Dimitri Kaparkov. "Empirical model of the microwave properties of high-temperature superconductors." Microwave Theory and Techniques, IEEE Transactions on 46.5 (1998): 469-478.

[29] S Kumar, J Gao, J Zmuidzinas, B A Mazin, H G LeDuc, and P K Day, Appl. Phys. Lett.

[30] Pappas, David P., et al. "Two level system loss in superconducting microwave resonators." Applied Superconductivity, IEEE Transactions on 21.3 (2011): 871-874.

[31] Phillips, W. A. "Two-level states in glasses." Reports on Progress in Physics 50.12 (1987): 1657.

[32] U. Strom, M. Schickfus, and S. Hunklinger, “Low-Temperatures Anomalies in the Microwave Dielectric Properties of Na -Alumina,” Phys. Rev. Lett., vol. 41, p. 910, 1978

[33] Luomahaara, Juho, et al. "Kinetic inductance magnetometer." Nature communications 5 (2014).

[34] Zmuidzinas, Jonas, et al. "Multiplexable kinetic inductance detectors."Proceedings Far-IR, Sub–mm, and MM Detector Workshop, eds. J. Wolf, J. Farhoomand, and CR McCreight, NASA/CP-2003-211408. 2002.

[35] Eom, Byeong Ho, et al. "A wideband, low-noise superconducting amplifier with high dynamic range." Nature Physics 8.8 (2012): 623-627.

[36] Meservey, R., and P. M. Tedrow. "Measurements of the kinetic inductance of superconducting linear structures." Journal of Applied Physics 40.5 (1969): 2028-2034.

[37] Anlage, S. M., H. J. Snortland, and M. R. Beasley. "A current controlled variable delay superconducting transmission line." Magnetics, IEEE Transactions on 25.2 (1989): 1388-1391.

[38] Tao, D. J., et al. "Czochralski growth of $(La, Sr)(Al, Ta)O_3$ single crystal." Optical Materials 23.1 (2003): 425-428.

[39] Tidrow, S. C., et al. "New substrates for HTSC microwave devices." Applied Superconductivity, IEEE Transactions on 7.2 (1997): 1766-1768.

[40] Koelle, D., et al. "High-transition-temperature superconducting quantum interference devices." Reviews of Modern Physics 71.3 (1999): 631.

A

Characterization of YBCO thin films

To investigate the quality of the thin film of YBCO, validate certain fabrication process steps and to examine the achieved resonator design, several characterisation techniques were used.

A.1 Scanning electron microscopy (SEM)

A scanning electron microscope (SEM) is a type of electron microscope that uses focused beam of high energy electrons to scan and produces images of a sample. The signals from this electron-surface interaction reveals information about the external morphology (texture) of the sample, chemical composition, and crystalline structure of the material being scanned. SEM has a greater "depth of field" or magnification than conventional optical microscopes. Here, SEM was used to determine the morphology of the test samples and to verify that (103) oriented YBCO had been produced. The electrons were fired at a voltage of 5 kV and several different magnifications were used, ranging from 104 to 105 times magnification.

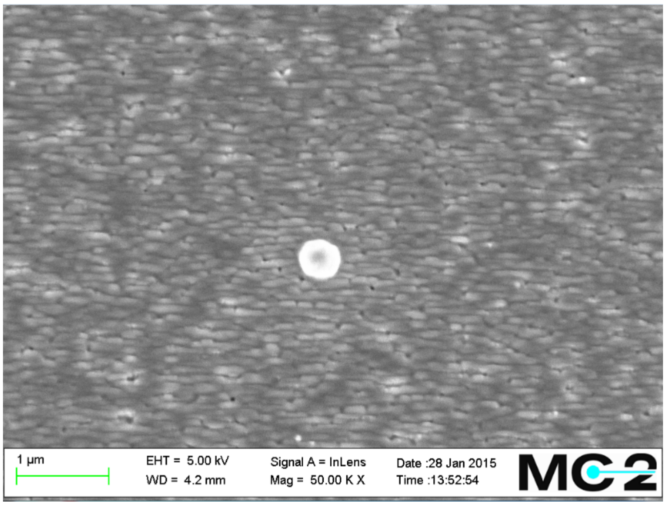

Figure A.1: SEM image of YBCO deposited using CALAS system. The dust particle is used to focus the electron beam on the surface.

As can be seen in Figure A.1, the samples shows detailed morphology of the film and it is confirmed that (103) oriented YBCO was grown during PLD.

A.2 X-Ray diffractometry (XRD)

An X-ray crystallography tool was used to assess the quality of the YBCO and verify its crystalline structure. XRD relies on the wave-particle nature of X-rays to obtain information about the crystalline structure. The interaction of the X-rays with the sample can be described by *Bragg's equation*:

$$n\lambda = 2d \sin\theta \tag{A.1}$$

X-ray diffraction using can be applied to many different types of applications including thin film analysis, sample texture evaluation, monitoring of crystalline structure, and investigation of stress and strain in the sample.

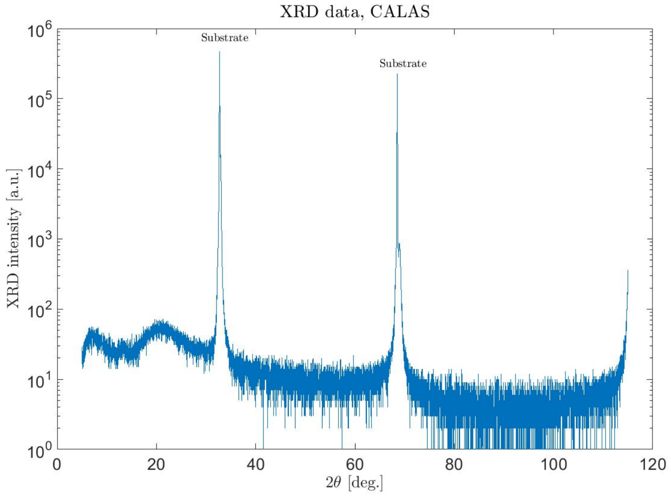

Figure A.2: XRD data from YBCO sample.

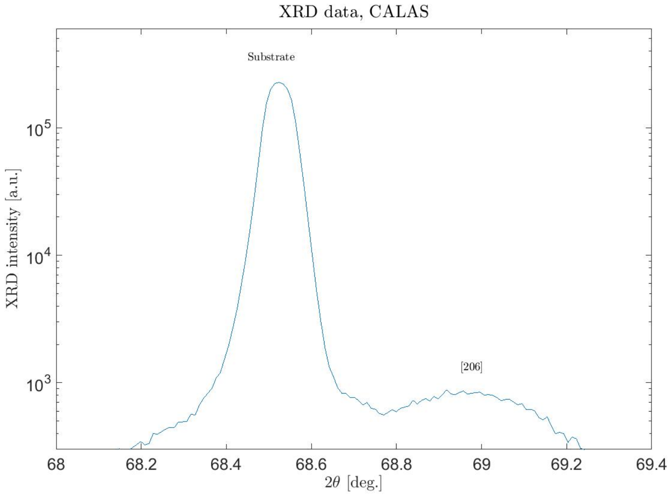

[H]

Figure A.3: A zoomed in version of Figure A.2, showing the peak separation at 68°.

As can be seen in Figure A.2, large peaks were observed at 32.72° and 68.52° and smaller peaks at 32.89° and 68.99°. By comparing these peaks to the values in database, it is confirmed that the large peaks correspond to LSAT [n n 0] and the smaller peaks correspond to YBCO [n 0 3n]. Since there is no peak corresponding to YBCO [0 0 n] present, it is confirmed that primarily (103) YBCO growth was achieved and not (001) growth.

Due to the vicinal cut, the YBCO and LSAT substrate are oriented differently. This is resolved by varying both angles, 2θ and ω, resulting in a 2D contour map.

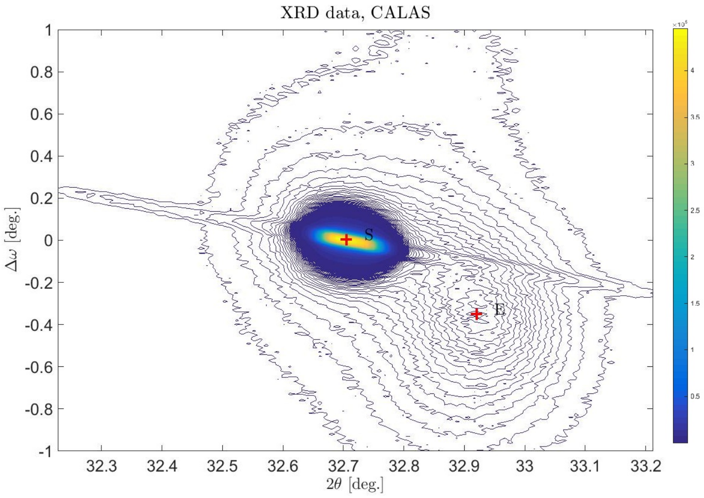

Figure A.4: XRD data using $\theta - 2\theta$ scan for the YBCO sample.

From Figure A.4, it is noted that there is a wide separation between the two peaks S and E. The difference in omega is explained by the vicinal cut. Also, it is noted that the shape of the peaks are rather different: from Figure A.4 it is clear that the substrate peak is sharp, but the peak corresponding to the (103) YBCO is broader. This is due to a uniform structure in the substrate, whereas growth of the (103) YBCO has not been as uniform.

A.3 Profilometry

To confirm that the etching processes for the gold frame, a profilometer was used. Using this instrument, the surface contour of the sample was mapped and authenticated.

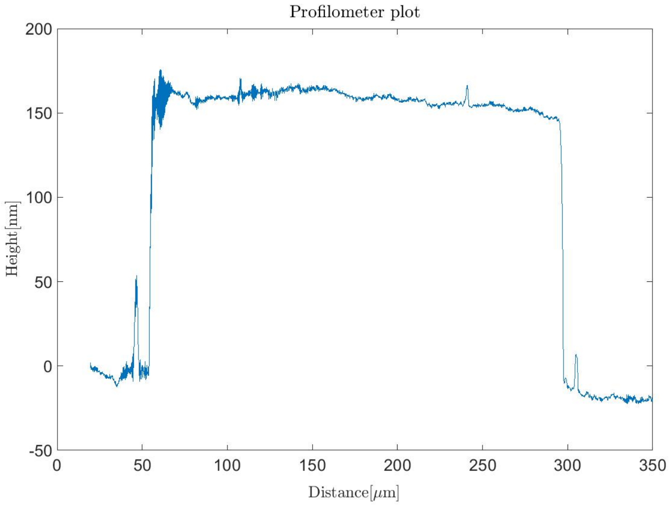

Figure A.5: A picture of the gold frame using the profilometer.

As can be seen in Figure A.5, a gold frame with a height of approximately 150 nm and a width of approximately 240 μm was produced.

A.4 Secondary ion mass spectroscopy (SIMS)

SIMS was used during the second argon ion etching step to confirm that the etching removed all the YBCO and reached down to the substrate layer in the desired places.

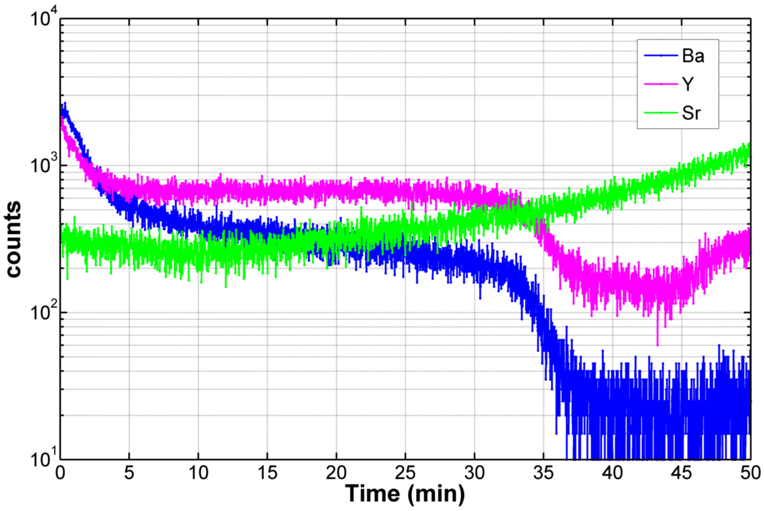

Figure A.6: SIMS data from the second argon ion etching step.

Figure A.6 shows an increase in the signal from strontium (which is only present in LSAT) and a decrease of the signal from yttrium and barium (which are present in the YBCO layer), which suggests that the YBCO was etched in desired places and that the argon ions reach the substrate.

The SIMS cannot alone show whether all YBCO has been etched in all gaps. Therefore, a probe station was used later to measure the resistance across different parts of the device and thereby confirming that no YBCO was present.

B

Recipes

B.1 Spinner parameters for the deposition of the photoresist.

Rotation speed (r.p.m)	7000
Acceleration time (s)	3
Time at maximum rotation speed (s)	90
Deceleration time (s)	3

B.2 Parameters for the first Ar ion etching step.

Angle (°)	-5
Base pressure (mbar)	$3.0*10^{-7}$
Ar flow (ml/min)	4.00
Current (mA)	7,6
Current density (mA/cm^2)	0.078
Process pressure (mbar)	$1.3*10^{-4}$
Neutraliser	OFF

B.3 Parameters used in the oxygen plasma treatment.

Oxygen flow (ml/min)	10
Pressure (mTorr)	250
Power (W)	50

B.4 Parameters used in the second etching step.

Beam voltage (V)	300
Acceleration voltage (V)	300
Beam current (mA)	8
Current density (mA/cm^2)	0.14
Tilt (°)	5
Neutraliser beam current (mA)	200
Neutraliser Ar flow (ml/min)	5
Etching Ar flow (ml/min)	3

B.5 Parameters used in the final etching step.

Beam current (mA)	5
Beam voltage (V)	300
Acceleration voltage (V)	300
Neutraliser current (mA)	200
Beam current density (mA/cm^2)	0.09

C

Determining the resonator responsivity

The responsivity of the magnetometer is calculated from $\frac{\partial v_{out}}{\partial B}$, where v_{out} is the reflected voltage and B is the applied magnetic field. At resonance, the responsivity can be approximated as:

$$\left|\frac{\partial v_{out}}{\partial B}\right|_{f=f_0} = \left|\frac{\partial v_{out}}{\partial L_{kin}}\frac{\partial L_{kin}}{\partial I_s}\frac{\partial I_s}{\partial B}\right|_{f=f_0} \tag{C.1}$$

The complex valued reflection signal around f_0 is given by the expression:

$$\Gamma = \frac{V_{out}}{V_{in}} = \frac{Q_{ext}^{-1} - Q_0^{-1} - 2i\delta x}{Q_{ext}^{-1} + Q_0^{-1} + 2i\delta x} \tag{C.2}$$

with $\delta x = \frac{f-f_0}{f_0}$. Consider the resonator is in the critical coupling regime, $Q_{ext} = Q_0 = Q$. Differentiating the above equation,

$$\left|\frac{\partial v_{out}}{\partial L_k}\right|_{f=f_0} = \frac{V_{in}Q}{2(L_{kin} + L_{geo})} \tag{C.3}$$

Differentiating Equation 1.39, one gets

$$\left|\frac{\partial L_{kin}}{\partial I_s}\right|_{f=f_0} = 2L_{kin,0}\frac{I_s}{I^*} \tag{C.4}$$

It is also know that $L_{tot}I_s = BA_{eff}$. Differentiating this equation, one gets

$$\left|\frac{\partial I_s}{\partial B}\right|_{f=f_0} = \frac{A_{eff}}{L_{tot}} = \frac{A_{eff}}{(L_{kin} + L_{geo})} \tag{C.5}$$

Combining Equations C.3, C.4 and C.5

$$\left|\frac{\partial v_{out}}{\partial B}\right|_{f=f_0} = V_{in}Q\frac{I_s}{(I^*)^2}\frac{L_{kin,0}}{L_{tot}}A_{eff} \tag{C.6}$$